

Revisiting the Austral Spring Extratropical Southern Hemisphere zonally asymmetric circulation using complex Empirical Orthogonal Functions

Elio Campitelli^{1,2,3*}, Leandro B. Díaz^{1,2,3} and Carolina
Vera^{1,2,3}

¹*Universidad de Buenos Aires, Facultad de Ciencias Exactas y
Naturales, Departamento de Ciencias de la Atmósfera y los
Océanos, Buenos Aires, Argentina.

²*CONICET – Universidad de Buenos Aires. Centro de
Investigaciones del Mar y la Atmósfera (CIMA), Buenos Aires,
Argentina.

³CNRS – IRD – CONICET – UBA. Instituto Franco-Argentino
para el Estudio del Clima y sus Impactos (IRL 3351 IFAECI),
Buenos Aires, Argentina.

*Corresponding author(s). E-mail(s):
elio.campitelli@cima.fcen.uba.ar;

Abstract

The large-scale extratropical circulation in the Southern Hemisphere is much more zonally symmetric than that of the Northern Hemisphere, but its zonal departures, albeit highly relevant for regional impacts, have been less studied. In this study we analyse the joint variability of the zonally asymmetric springtime stratospheric and tropospheric circulation using Complex Empirical Orthogonal Functions (cEOF) to characterise planetary waves of varying amplitude and phase. The leading cEOF represents variability of a zonal wave 1 in the stratosphere that correlates slightly with the Symmetric Southern Annular Mode (S-SAM). The second cEOF (cEOF2) is an alternative representation of the Pacific-South American modes. One phase of this cEOF is also extremely correlated with the Asymmetric SAM (A-SAM)

2 SH zonally asymmetric circulation with cEOF

047 in the troposphere. Springs with an active ENSO tend to phase-lock
 048 the cEOF2, but have no consistent impact on its magnitude. Fur-
 049 thermore, we find indications that the location of Pacific Sea Surface
 050 Temperature anomalies affect the phase of the cEOF2. As a result, the
 051 methodology proposed in this study provides a deeper understanding
 052 of the zonally asymmetric springtime extratropical SH circulation.

053 **Keywords:** Southern Hemisphere circulation, Teleconnections, Pacific South
 054 American Mode, Southern Annular Mode, Stratosphere

058 1 Introduction

introduction

060 The large-scale extratropical circulation in the Southern Hemisphere (SH) is
 061 much more zonally symmetric than that of the Northern Hemisphere, but
 062 departures from the zonal mean are associated with regional impacts (e.g.
 063 [Hoskins and Hedges, 2005](#)). They strongly modulate weather systems and
 064 regional climate through promoting longitudinally varying meridional trans-
 065 port of heat, humidity, and momentum ([Trenberth, 1980](#); [Raphael, 2007](#)) and
 066 could even be related to the occurrence of high-impact climate extremes ([Pezza](#)
 067 [et al, 2012](#)).

068 The zonally asymmetric circulation is typically described by the amplitude
 069 and phase of zonal waves obtained by Fourier decomposition of geopotential
 070 height or sea-level pressure at each latitude (e.g. [van Loon and Jenne, 1972](#);
 071 [Trenberth, 1980](#); [Turner et al, 2017](#)). This approach suggests that zonal waves
 072 1 and 3 explain almost 99% of the total variance in the annual mean 500 hPa
 073 geopotential height zonal anomalies at 50°S ([van Loon and Jenne, 1972](#)). [Tren-](#)
 074 [berth and Mo \(1985\)](#) concluded that wave 3 plays a role in the development
 075 of blocking events. In addition, previous works have identified wave-like pat-
 076 terns with dominant wavenumbers 3-4 at extratropical and subpolar latitudes
 077 with distinctive regional impacts. [Raphael \(2007\)](#) showed that variability in
 078 the planetary wave 3 projected onto its climatological location is associated
 079 with anomalies in the Antarctic sea-ice concentration.

080 Fourier decomposition relies on the assumption that the circulation can be
 081 meaningfully described in terms of zonal waves of constant amplitude along a
 082 latitude circle. However, this is not valid for meridionally propagating waves or
 083 zonal waves with localised amplitudes. Addressing this limitation, the Fourier
 084 technique can be generalized to integrate all planetary wave amplitude regard-
 085 less of wave number by computing the wave envelope ([Irving and Simmonds,](#)
 086 [2015](#)). The wave envelope can represent planetary waves with different ampli-
 087 tude at different longitudes, but lacks information about phase and wave
 088 number. Using this method, [Irving and Simmonds \(2015\)](#) showed that plane-
 089 tary wave amplitude in general is associated to Antarctic sea-ice concentration
 090 and temperature, as well as to precipitation anomalies in regions of significant
 091 topography in SH mid-latitudes and Antarctica.

Another extensively-used approach to characterise the SH tropospheric circulation anomalies, is computing Empirical Orthogonal Functions (EOF, also known as Principal Component Analysis). Within the EOF framework, the Southern Annular Mode (SAM) appears as the leading mode of variability of the SH circulation (Fogt and Marshall, 2020). The SAM represents a relatively zonally symmetric pattern of alternating low pressures in polar latitudes and a ring of high pressures in high latitudes with an embedded wave 3 pattern that is more prominent in the Pacific sector. The 2nd and 3rd EOFs, usually known as Pacific–South American Patterns (PSA) 1 and PSA2 patterns, respectively, describe meridionally propagating wave trains that originate in the eastern equatorial Pacific and Australian-Indian Ocean sector, and travel towards the South Atlantic following a great-circle arch along the Antarctic coast (Mo and Paegle, 2001). These patterns influence precipitation anomalies in South America (Mo and Paegle, 2001). Although these patterns are usually derived by applying EOF to temporal anomalies, Raphael (2003) also applied EOF methods specifically to zonal anomalies. Irving and Simmonds (2016) proposed a novel methodology for objectively identifying the PSA pattern using Fourier decomposition. More recently Goyal et al (2022) created an index of amplitude and phase of zonal wave 3-like variability by combining the two leading EOFs of meridional wind anomalies.

Some of the zonally asymmetric patterns of the SH circulation variability described previously appear to have experienced secular changes. For instance, Raphael (2003) suggests that the amplitude of the zonal wave 1 experienced a large increase and that the zonal wave 3 experienced changes in its annual cycle between 1958 and 1996. However, little is known yet about variability and trends of these patterns.

Patterns resulting from EOF analysis are more flexible than Fourier decomposition-derived modes in that they can capture oscillation patterns that cannot be characterised by purely sinusoidal waves with constant amplitude. Nonetheless, they are restricted to standing oscillation modes and cannot properly represent propagating or phase-varying features such as zonal waves. A single EOF can also represent a mixture of two or more physical modes.

A third methodology commonly used to describe circulation anomalies consists on identifying particular features of interest and creating indices using simple methods such as averages and differences. Examples of this methodology are the SAM Index of Gong and Wang (1999), the SH wave 3 activity index defined by Raphael (2004) and the SH zonally asymmetric circulation index from Hobbs and Raphael (2010). These derived methods are grounded on other methods such as Fourier decomposition or EOF to identify the centres of action for the described phenomena and can be useful to characterise features that are not readily apparent with these methods. These kinds of indices are generally easy to compute, but they usually do not capture non-stationary patterns.

An alternative methodology that has been proposed to study travelling and standing waves is complex Empirical Orthogonal Functions (cEOF; Horel

4 SH zonally asymmetric circulation with cEOF

139 (1984)). This method extends EOF analysis to capture oscillations with vary-
 140 ing amplitude and phase and has been applied to the time domain. For
 141 instance, Krokkin and Luxemburg (2007) applied cEOF to station-based
 142 monthly precipitation anomalies and monthly temperature anomalies in the
 143 Eastern Siberia and the Far East region to characterise the main modes of vari-
 144 ability and their relationship with teleconnection indices. Similarly, Gelbrecht
 145 et al (2018) applied cEOF to daily precipitation from reanalysis to study the
 146 propagating characteristics of the South American Monsoon. To our knowl-
 147 edge, cEOF analysis has not been applied in the spatial domain to capture
 148 the phase-varying nature of planetary waves in the atmosphere.

149 The general goal of this study is to improve the description and under-
 150 standing of the zonally asymmetric extratropical SH circulation using cEOF,
 151 which can describe phase varying planetary waves with variable amplitude
 152 along a latitude circle. In addition, we try to expand the knowledge of the
 153 simultaneous behaviour of SH asymmetric circulation in the troposphere and
 154 the stratosphere.

155 We restrict this work to the September-October-November (SON)
 156 trimester because during this season both the tropical teleconnections
 157 over South America (Cazes-Boezio et al, 2003) and the SH stratosphere-
 158 troposphere interactions (Lim et al, 2018) are at their maximum amplitude.

159 In Section 2 we describe the methods. In Section 3.1 we analyse the spatial
 160 patterns of each complex EOF. In Section 3.2 we study the spatial regressions
 161 with geopotential height, temperature and ozone anomalies. In Section 3.3 and
 162 3.4 we analyse the relationship between cEOF2, the PSA and SAM modes. In
 163 Section 3.5 we study tropical forcings that explain the variability of each cEOF.
 164 In Section 3.6 we show the relationship between these modes of variability
 165 and precipitation and surface temperature anomalies in South America and
 166 Oceania. In Section 4 we compare our results with previous studies and discuss
 167 the benefits of our methodology.

168

169 2 Data and Methods

170

171 2.1 Data

172

173 We used monthly geopotential height, air temperature, ozone mixing ratio,
 174 and total column ozone (TOC) at 2.5° longitude by 2.5° latitude of hori-
 175 zontal resolution and 37 vertical isobaric levels from the European Centre for
 176 Medium-Range Weather Forecasts Reanalysis version 5 [ERA; Hersbach et al
 177 (2019)] for the period 1979 – 2019. Most of our analysis is restricted to the
 178 post-satellite era to avoid confounding factors arising from the incorporation
 179 of satellite observations, but we also used the preliminary back extension of
 180 ERA5 from 1950 to 1978 (Bell et al, 2020) to describe long-term trends. We
 181 derived streamfunction at 200 hPa from ERA5 vorticity using the FORTRAN
 182 subroutine FISHPACK (Adams et al, 1999) and we computed horizontal
 183 wave activity fluxes following Plumb (1985). Sea Surface Temperature (SST)
 184 monthly fields are from Extended Reconstructed Sea Surface Temperature

methods

data

(ERSST) v5 (Huang et al, 2017) and precipitation monthly data from the CPC Merged Analysis of Precipitation (CMAP, Xie and Arkin, 1997), with a 2° and 2.5° horizontal resolution, respectively. The rainfall gridded dataset is based on information from different sources such as rain gauge observations, satellite inferred estimations and the NCEP-NCAR reanalysis, and it is available from 1979 to the present.

The Oceanic Niño Index (ONI, Bamston et al, 1997) comes from NOAA's Climate Prediction Center and the Dipole Mode Index (DMI, Saji and Yamagata, 2003) from Global Climate Observing System Working Group on Surface Pressure.

2.2 Methods

The study is restricted to the spring season, defined as the September-October-November (SON) trimester. We compute seasonal means for the different variables, averaging monthly values weighted by the number of days in each month. We use the 200 hPa level to represent the high troposphere and 50 hPa to represent the lower stratosphere.

We computed the amplitude and phase of the TOC wave 1 by averaging (area-weighted) the data of each SON between 75°S and 45°S , and then extracting the wave-1 component of the Fourier spectrum. We chose this latitude band because it is wide enough to capture most of the relevant anomalies of SH mid-latitudes.

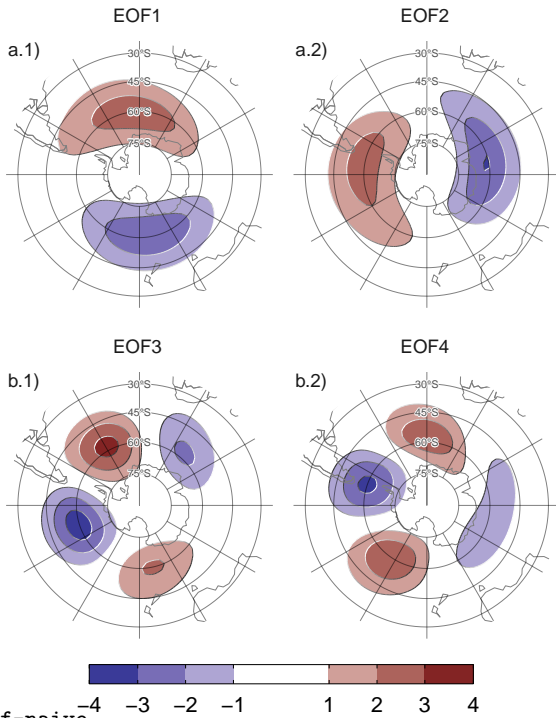
We computed the level-dependent SAM index as the leading EOF of year-round monthly geopotential height anomalies south of 20°S at each level for the whole period (Baldwin and Thompson, 2009). We further split the SAM into its zonally symmetric and zonally asymmetric components (S-SAM and A-SAM indices respectively). These indices were obtained by projecting monthly geopotential height fields onto the zonally asymmetric and zonally symmetric parts of the SAM spatial pattern, as proposed by Campitelli et al (2022b). Seasonal indices of the PSA patterns (PSA1 and PSA2) were calculated, in agreement with Mo and Paegle (2001), as the third and fourth EOFs of seasonal mean anomalies for 500-hPa geopotential heights at SH.

Linear trends were computed by Ordinary Least Squares (OLS) and the 95% confidence interval was computed assuming a t-distribution with the appropriate residual degrees of freedom (Wilks, 2011).

2.3 Complex Empirical Orthogonal Functions (cEOF)

In the standard EOF analysis, zonal waves may appear as pairs of (possibly degenerate) EOFs representing similar patterns but shifted in phase (Horel, 1984). Figure 1 shows the four leading EOFs of SON geopotential height zonal anomalies at 50 hPa south of 20°S . It is clear that the first two EOFs represent a single phase-varying zonal wave 1 pattern and the last two represent a similarly phase-varying pattern with higher wavenumber and three centres of action shifted by $1/4$ wavelength (90° in frequency space).

	185
	186
	187
	188
	189
	190
	191
	192
	193
	194
	195
methods-1	196
	197
	198
	199
	200
	201
	202
	203
	204
	205
	206
	207
	208
	209
	210
	211
	212
	213
	214
	215
	216
	217
	218
	219
	220
	221
	222
	223
	224
	225
	226
	227
	228
	229
	230

6 *SH zonally asymmetric circulation with cEOF*231
232
233
234
235
236
237
238
239
240

251
252 **Fig. 1:** Spatial patterns of the four leading EOFs of SON geopotential height
253 zonal anomalies at 50 hPa south of 20° S for the 1979 – 2019 period (arbitrary
254 units).
255

256
257

258 To describe the phase-varying nature of these two wave patterns, one way
259 is to combine each pair of EOFs into indices of amplitude and phase. So,
260 for instance, the amplitude of the wave 1-like EOF could be measured as
261 $\sqrt{PC1^2 + PC2^2}$ and its phase as $\tan^{-1}(\frac{PC2}{PC1})$ (where PC1 and PC2 are the
262 time series associated with each EOF). However, this rests on visual inspection
263 of the spatial patterns and only works properly if both phases appear clearly
264 in different EOFs, which is not guaranteed by construction. In particular, this
265 does not work with the wave 1 pattern depicted as the leading EOF in 200
266 hPa geopotential height zonal anomalies (not shown).
267

268 On the other hand, a better alternative for describing phase-varying waves
269 is to use Complex Empirical Orthogonal Functions (cEOF) analysis (Horel,
270 1984). Each cEOF is a set of complex-valued spatial patterns and time series.
271 The real and imaginary components of the complex spatial pattern can be
272 thought of as representing two spatial patterns that are shifted by 1/4 wave-
273 length by construction, similar to EOF1 and EOF2 in Figure 1. In this paper
274 we use the term 0° cEOF and 90° cEOF to refer to each part of the whole
275 cEOF. The actual field reconstructed by each cEOF is then the linear combi-
276 nation of the two spatial fields weighted by its respective time series. This

Table 1: tab:corr-ceof-splitted Coefficient of determination (r^2) between the time series of the absolute magnitude of complex EOFs computed separately at 200 hPa and 50 hPa (p-values lower than 0.01 in bold).

		50 hPa		
		cEOF1	cEOF2	cEOF3
200 hPa				
cEOF1	0.29	0.01	0.03	
cEOF2	0.00	0.59	0.02	
cEOF3	0.00	0.00	0.01	

is analogous to how any sine wave can be constructed by the sum of a sine wave and cosine wave with different amplitude but constant phase. This means that cEOFs naturally represent phase-varying wave-like patterns that change location as well as amplitude.

For instance, when the phase of the wave matches the 0° phase, then the 0° phase time series is positive and the 90° phase time series is zero. Similarly, when the phase of the wave matches the 90° phase, the 90° phase time series is positive and the 0° phase time series is zero. The intermediate phases have non-zero values in both time series.

Traditional EOFs are not unique, and instead are defined up to sign, which corresponds to a rotation in the complex plane of either 0 or π . In the same way, cEOFs are defined up to a rotation in the complex plane of any value between 0 and 2π (Horel, 1984).

cEOFs are computed in the same way as traditional EOFs except that the data is first augmented by computing its analytic signal. This is a complex number whose real part is the original series and whose imaginary part is the original data shifted by 90° at each spectral frequency – i.e. its Hilbert transform. The Hilbert transform is usually understood in terms of time-varying signal. However, in this work we apply the Hilbert transform at each latitude circle and at each considered time (i.e. the signal only depends on longitude). Since each latitude circle is a periodic domain, this procedure does not suffer from edge effects.

We first applied cEOF analysis to geopotential height zonal anomalies south of 20°S at 50 and at 200 hPa. Figure 2 a.1 shows the spatial patterns of the two leading cEOF. The 0° phase is plotted with shaded contours and the 90° phase, with black contours. The two phases of the leading cEOF are very similar to the two leading EOFs shown in Figure 1 and represent a zonal wave 1 pattern; the 0° phase is roughly the EOF1 and the 90° phase is roughly the EOF2).

Table 1 shows the coefficient of determination between time series of the amplitude of each cEOF across levels. There is a high degree of correlation between the magnitude of the respective cEOF1 and cEOF2 at each level. The spatial patterns of the 50 hPa and 200 hPa cEOFs are also similar (not shown).

8 *SH zonally asymmetric circulation with cEOF*

323 Both the spatial pattern similarity and the high temporal correlation of
 324 cEOFs computed at 50 hPa and 200 hPa suggest that these are, to a large
 325 extent, modes of joint variability. This motivates the decision of performing
 326 cEOF jointly between levels. Therefore cEOFs were computed using data from
 327 both levels at the same time. In that sense each cEOF has a spatial component
 328 that depends on longitude, latitude and level, and a temporal component that
 329 depends only on time.

330 As mentioned before, the choice of phases is arbitrary and equally valid.
 331 But to make the interpretation easier, we chose the phase of each cEOF so
 332 that either the 0° cEOF or the 90° cEOF is aligned with meaningful variables
 333 in our analysis. This procedure does not create spurious correlations, it only
 334 takes an existing relationship and aligns it with a specific phase.

335 Preliminary analysis showed that the first cEOF was closely related to the
 336 zonal wave 1 of TOC and the second cEOF was closely related to ENSO.
 337 Therefore, we chose the phase of cEOF1 so that the time series corresponding
 338 to the 0° cEOF1 has the maximum correlation with the zonal wave 1 of TOC
 339 between 75°S and 45°S. Similarly, we chose the phase of cEOF2 so that the
 340 coefficient of determination between the ONI and the 0° cEOF2 is minimised,
 341 which also nearly maximises the correlation with the 90° cEOF2.

342 In Section 3.6 we show regressions of precipitation and temperature associated
 343 with intermediate phases. For those plots, we rotated the cEOFs by 1/4
 344 wavelength by multiplying the complex time series by $\cos(\pi/4) + i \sin(\pi/4)$
 345 and computing the regression on those rotated timeseries.

346 While we compute these complex principal components using data from
 347 1979 to 2019, we extended the complex time series back to the 1950 – 1978
 348 period by projecting monthly geopotential height zonal anomalies standardised
 349 by level south of 20°S onto the corresponding spatial patterns.

350 We performed linear regressions to quantify the association between the
 351 cEOFs and other variables (e.g. geopotential height, temperature, precipitation,
 352 and others). For each cEOF, we computed regression maps by fitting a
 353 multiple linear model involving both the 0° and the 90° phases. To obtain the
 354 linear coefficients of a variable X with the 0° and 90° phase of each cEOF we
 355 fit the equation

356

357

$$358 X(\lambda, \phi, t) = \alpha(\lambda, \phi) \text{cEOF}_0 + \beta(\lambda, \phi) \text{cEOF}_{90} + X_0(\lambda, \phi) + \epsilon(\lambda, \phi, t)$$

359

360 where λ and ϕ are the longitude and latitude, t is the time, α and β are
 361 the linear regression coefficients for 0° and 90° phases respectively, X_0 and ϵ
 362 are the constant and error terms respectively.

363 We evaluated statistical significance using a two-sided t-test and, in the
 364 case of regression maps, p-values were adjusted by controlling for the False
 365 Discovery Rate (Benjamini and Hochberg, 1995; Wilks, 2016) to avoid mis-
 366 leading results from the high number of regressions (Walker, 1914; Katz and
 367 Brown, 1991).

368

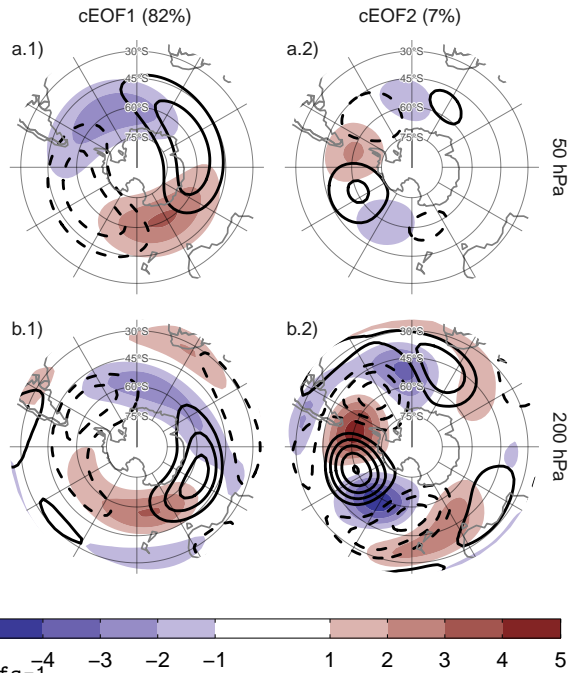


Fig. 2: Spatial patterns for the two leading cEOFs of SON geopotential height zonal anomalies at 50 hPa and 200 hPa for the 1979 – 2019 period. The shading (contours) corresponds to 0° (90°) phase. Arbitrary units. The proportion of variance explained for each mode with respect to the zonal mean is indicated in parenthesis.

2.4 Computation procedures

We performed all analysis in this paper using the R programming language ([R Core Team, 2020](#)), using `data.table` ([Dowle and Srinivasan, 2020](#)) and `metR` ([Campitelli, 2020](#)) packages. All graphics are made using `ggplot2` ([Wickham, 2009](#)). We downloaded data from reanalysis using the `ecmwf.r` package ([Hufkens, 2020](#)) and indices of ENSO and Indian Ocean Dipole (IOD) with the `rsoi` package ([Albers and Campitelli, 2020](#)). The paper was rendered using `knitr` and `rmarkdown` ([Xie, 2015; Allaire et al, 2020](#)).

3 Results

3.1 cEOF spatial patterns

To describe the variability of the circulation zonal anomalies, the spatial and temporal parts of the first two leading cEOFs of zonal anomalies of geopotential height at 50 hPa and 200 hPa, computed jointly at both levels, are shown in Figures 2 and 3. The first mode (cEOF1) explains 82% of the variance of the zonally anomalous fields, while the second mode (cEOF2) explains a smaller

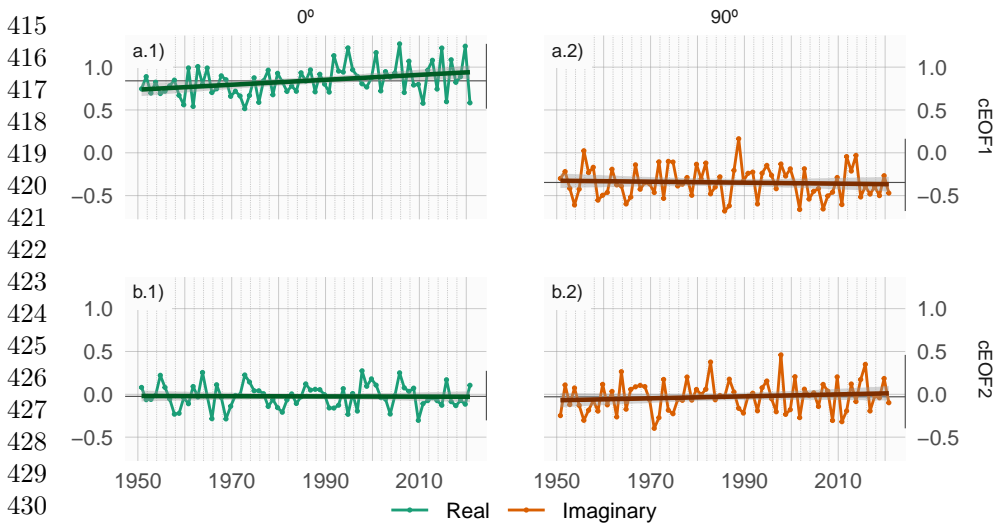
10 *SH zonally asymmetric circulation with cEOF*

Fig. 3: Time series of the two leading cEOFs of SON geopotential height zonal anomalies at 50 hPa and 200 hPa. cEOF1 (row a) and cEOF2 (row b) separated in their 0° (column 1) and 90° (column 2) phase. Dark straight line is the linear trend. Black horizontal and vertical line mark the mean value and range of each time series.

fig:extended-series

fraction (7%). In the spatial patterns (Fig. 2), the 0° and the 90° phases are in quadrature by construction, so that each cEOF describe a single wave-like pattern whose amplitude and position (i.e. phase) is controlled by the magnitude and phase of the temporal cEOF. The wave patterns described by these cEOFs match the patterns seen in the standard EOFs of Figure 1.

The cEOF1 (Fig. 2 column 1) is a hemispheric wave 1 pattern with maximum amplitude at high latitudes. At 50 hPa the 0° cEOF1 has the maximum of the wave 1 at 150°E and at 200 hPa, the maximum is located at around 175°E indicating a westward shift with height. The cEOF2 (Fig. 1 column 2) shows also a zonal wave-like structure with maximum amplitude at high latitudes, but with shorter spatial scales. In particular, the dominant structure at both levels is a wave 3 but with larger amplitude in the pacific sector. There is no apparent phase shift with height but the amplitude of the pattern is greatly reduced in the stratosphere, which is consistent with the fact that the cEOF2 computed separately for 200 hPa explains a bit more variance than the cEOF2 computed separately for 50 hPa (11% vs. 3%, respectively). This suggest that this barotropic mode represents mainly tropospheric variability.

There is no significant simultaneous correlation between cEOFs time series. Both cEOFs show year-to-year variability but show no evidence of decadal variability (Fig. 3). Because the geopotential fields that enter into the cEOFs algorithm are anomalies with respect to the zonal mean instead of the time mean, the cEOFs time series have non zero temporal mean. However, cEOF2

temporal mean is almost zero, which indicates that only cEOF1 includes variability that significantly projects onto the mean zonally anomalous field. This is consistent with the fact that the mean zonally anomalous field of geopotential height is very similar to the cEOF1 ($r^2 = 98\%$) and not similar to the cEOF2 ($r^2 = 0\%$). 461
462
463
464
465

A significant positive trend in the 0° phase of cEOF1 is evident (Fig. 3a.1, p-value = 0.0037) while there is no significant trend in any of the phases of cEOF2. The positive trend in the 0° cEOF1 translates into a positive trend in cEOF1 magnitude, but not systematic change in phase (not shown). This long-term change indicates an increase in the magnitude of the high latitude zonal wave 1. 466
467
468
469
470
471
472
473
474
475
476
477
478
479
480

3.2 cEOFs Regression maps

regressions

3.2.1 Geopotential

geopotential

In the previous section, cEOF analysis was applied to zonal anomalies derived by removing the zonally mean values in order to isolate the main characteristics of the main zonal waves characterizing the circulation in the SH. In this section we compute regression fields using the full fields of the variables in order to describe the influence of the cEOFs on the temporal anomalies. 481
482
483
484
485
486
487
488
489
490
491
492
493
494
495
496
497
498
499
500
501
502

Figure 4 shows regression maps of SON geopotential height anomalies upon cEOF1. At 50 hPa (Figure 4 row a), the 0° cEOF1 is associated with a positive centre located over the Ross Sea. The 90° cEOF1 is associated with a distinctive wave 1 pattern with maximum over the coast of East Antarctica. At 200 hPa (Figure 4 row b) the 0° cEOF1 shows a single centre of positive anomalies spanning West Antarctica surrounded by opposite anomalies in lower latitudes, with its centre shifted slightly eastward compared with the upper-level anomalies. The 90° cEOF1 shows a much more zonally symmetrical pattern resembling the negative SAM phase (e.g. Fogt and Marshall, 2020). Therefore, the magnitude and phase of the cEOF1 are associated with the magnitude and phase of a zonal wave mainly in the stratosphere. 503
504
505
506

Figure 5 shows the regression maps of geopotential height anomalies upon the cEOF2. In the troposphere (Fig. 5 row a) the regression maps show wave trains similar to those identified for cEOF2 patterns (Fig 2). Regressed anomalies associated with the 0° cEOF2 are 1/4 wavelength out of phase with those associated with the 90° cEOF2. All fields have a dominant zonal wave 3 limited to the western hemisphere, over the Pacific and Atlantic Oceans. cEOF2 then represents an equivalent barotropic wave train that is very similar to the the PSA Patterns (Mo and Paegle, 2001). Comparing the location of the positive anomaly near 90°W in column 2 of Figure 5 with Figures 1.a and b from Mo and Paegle (2001), the 0° cEOF2 regression map could be identified with PSA2, while the 90° cEOF2 resembles PSA1. 507
508
509
510
511
512
513
514
515
516
517
518
519
520
521
522
523
524
525
526
527
528
529
530
531
532
533
534
535
536
537
538
539
540
541
542
543
544
545
546
547
548
549
550
551
552
553
554
555
556
557
558
559
560
561
562
563
564
565
566
567
568
569
570
571
572
573
574
575
576
577
578
579
580
581
582
583
584
585
586
587
588
589
590
591
592
593
594
595
596
597
598
599
600
601
602
603
604
605
606
607
608
609
610
611
612
613
614
615
616
617
618
619
620
621
622
623
624
625
626
627
628
629
630
631
632
633
634
635
636
637
638
639
640
641
642
643
644
645
646
647
648
649
650
651
652
653
654
655
656
657
658
659
660
661
662
663
664
665
666
667
668
669
670
671
672
673
674
675
676
677
678
679
680
681
682
683
684
685
686
687
688
689
690
691
692
693
694
695
696
697
698
699
700
701
702
703
704
705
706
707
708
709
710
711
712
713
714
715
716
717
718
719
720
721
722
723
724
725
726
727
728
729
730
731
732
733
734
735
736
737
738
739
740
741
742
743
744
745
746
747
748
749
750
751
752
753
754
755
756
757
758
759
750
751
752
753
754
755
756
757
758
759
760
761
762
763
764
765
766
767
768
769
770
771
772
773
774
775
776
777
778
779
770
771
772
773
774
775
776
777
778
779
780
781
782
783
784
785
786
787
788
789
780
781
782
783
784
785
786
787
788
789
790
791
792
793
794
795
796
797
798
799
790
791
792
793
794
795
796
797
798
799
800
801
802
803
804
805
806
807
808
809
800
801
802
803
804
805
806
807
808
809
810
811
812
813
814
815
816
817
818
819
810
811
812
813
814
815
816
817
818
819
820
821
822
823
824
825
826
827
828
829
820
821
822
823
824
825
826
827
828
829
830
831
832
833
834
835
836
837
838
839
830
831
832
833
834
835
836
837
838
839
840
841
842
843
844
845
846
847
848
849
840
841
842
843
844
845
846
847
848
849
850
851
852
853
854
855
856
857
858
859
850
851
852
853
854
855
856
857
858
859
860
861
862
863
864
865
866
867
868
869
860
861
862
863
864
865
866
867
868
869
870
871
872
873
874
875
876
877
878
879
870
871
872
873
874
875
876
877
878
879
880
881
882
883
884
885
886
887
888
889
880
881
882
883
884
885
886
887
888
889
890
891
892
893
894
895
896
897
898
899
890
891
892
893
894
895
896
897
898
899
900
901
902
903
904
905
906
907
908
909
900
901
902
903
904
905
906
907
908
909
910
911
912
913
914
915
916
917
918
919
910
911
912
913
914
915
916
917
918
919
920
921
922
923
924
925
926
927
928
929
920
921
922
923
924
925
926
927
928
929
930
931
932
933
934
935
936
937
938
939
930
931
932
933
934
935
936
937
938
939
940
941
942
943
944
945
946
947
948
949
940
941
942
943
944
945
946
947
948
949
950
951
952
953
954
955
956
957
958
959
950
951
952
953
954
955
956
957
958
959
960
961
962
963
964
965
966
967
968
969
960
961
962
963
964
965
966
967
968
969
970
971
972
973
974
975
976
977
978
979
970
971
972
973
974
975
976
977
978
979
980
981
982
983
984
985
986
987
988
989
980
981
982
983
984
985
986
987
988
989
990
991
992
993
994
995
996
997
998
999
990
991
992
993
994
995
996
997
998
999
1000
1001
1002
1003
1004
1005
1006
1007
1008
1009
1000
1001
1002
1003
1004
1005
1006
1007
1008
1009
1010
1011
1012
1013
1014
1015
1016
1017
1018
1019
1010
1011
1012
1013
1014
1015
1016
1017
1018
1019
1020
1021
1022
1023
1024
1025
1026
1027
1028
1029
1020
1021
1022
1023
1024
1025
1026
1027
1028
1029
1030
1031
1032
1033
1034
1035
1036
1037
1038
1039
1030
1031
1032
1033
1034
1035
1036
1037
1038
1039
1040
1041
1042
1043
1044
1045
1046
1047
1048
1049
1040
1041
1042
1043
1044
1045
1046
1047
1048
1049
1050
1051
1052
1053
1054
1055
1056
1057
1058
1059
1050
1051
1052
1053
1054
1055
1056
1057
1058
1059
1060
1061
1062
1063
1064
1065
1066
1067
1068
1069
1060
1061
1062
1063
1064
1065
1066
1067
1068
1069
1070
1071
1072
1073
1074
1075
1076
1077
1078
1079
1070
1071
1072
1073
1074
1075
1076
1077
1078
1079
1080
1081
1082
1083
1084
1085
1086
1087
1088
1089
1080
1081
1082
1083
1084
1085
1086
1087
1088
1089
1090
1091
1092
1093
1094
1095
1096
1097
1098
1099
1090
1091
1092
1093
1094
1095
1096
1097
1098
1099
1100
1101
1102
1103
1104
1105
1106
1107
1108
1109
1100
1101
1102
1103
1104
1105
1106
1107
1108
1109
1110
1111
1112
1113
1114
1115
1116
1117
1118
1119
1110
1111
1112
1113
1114
1115
1116
1117
1118
1119
1120
1121
1122
1123
1124
1125
1126
1127
1128
1129
1120
1121
1122
1123
1124
1125
1126
1127
1128
1129
1130
1131
1132
1133
1134
1135
1136
1137
1138
1139
1130
1131
1132
1133
1134
1135
1136
1137
1138
1139
1140
1141
1142
1143
1144
1145
1146
1147
1148
1149
1140
1141
1142
1143
1144
1145
1146
1147
1148
1149
1150
1151
1152
1153
1154
1155
1156
1157
1158
1159
1150
1151
1152
1153
1154
1155
1156
1157
1158
1159
1160
1161
1162
1163
1164
1165
1166
1167
1168
1169
1160
1161
1162
1163
1164
1165
1166
1167
1168
1169
1170
1171
1172
1173
1174
1175
1176
1177
1178
1179
1170
1171
1172
1173
1174
1175
1176
1177
1178
1179
1180
1181
1182
1183
1184
1185
1186
1187
1188
1189
1180
1181
1182
1183
1184
1185
1186
1187
1188
1189
1190
1191
1192
1193
1194
1195
1196
1197
1198
1199
1190
1191
1192
1193
1194
1195
1196
1197
1198
1199
1200
1201
1202
1203
1204
1205
1206
1207
1208
1209
1200
1201
1202
1203
1204
1205
1206
1207
1208
1209
1210
1211
1212
1213
1214
1215
1216
1217
1218
1219
1210
1211
1212
1213
1214
1215
1216
1217
1218
1219
1220
1221
1222
1223
1224
1225
1226
1227
1228
1229
1220
1221
1222
1223
1224
1225
1226
1227
1228
1229
1230
1231
1232
1233
1234
1235
1236
1237
1238
1239
1230
1231
1232
1233
1234
1235
1236
1237
1238
1239
1240
1241
1242
1243
1244
1245
1246
1247
1248
1249
1240
1241
1242
1243
1244
1245
1246
1247
1248
1249
1250
1251
1252
1253
1254
1255
1256
1257
1258
1259
1250
1251
1252
1253
1254
1255
1256
1257
1258
1259
1260
1261
1262
1263
1264
1265
1266
1267
1268
1269
1260
1261
1262
1263
1264
1265
1266
1267
1268
1269
1270
1271
1272
1273
1274
1275
1276
1277
1278
1279
1270
1271
1272
1273
1274
1275
1276
1277
1278
1279
1280
1281
1282
1283
1284
1285
1286
1287
1288
1289
1280
1281
1282
1283
1284
1285
1286
1287
1288
1289
1290
1291
1292
1293
1294
1295
1296
1297
1298
1299
1290
1291
1292
1293
1294
1295
1296
1297
1298
1299
1300
1301
1302
1303
1304
1305
1306
1307
1308
1309
1300
1301
1302
1303
1304
1305
1306
1307
1308
1309
1310
1311
1312
1313
1314
1315
1316
1317
1318
1319
1310
1311
1312
1313
1314
1315
1316
1317
1318
1319
1320
1321
1322
1323
1324
1325
1326
1327
1328
1329
1320
1321
1322
1323
1324
1325
1326
1327
1328
1329
1330
1331
1332
1333
1334
1335
1336
1337
1338
1339
1330
1331
1332
1333
1334
1335
1336
1337
1338
1339
1340
1341
1342
1343
1344
1345
1346
1347
1348
1349
1340
1341
1342
1343
1344
1345
1346
1347
1348
1349
1350
1351
1352
1353
1354
1355
1356
1357
1358
1359
1350
1351
1352
1353
1354
1355
1356
1357
1358
1359
1360
1361
1362
1363
1364
1365
1366
1367
1368
1369
1360
1361
1362
1363
1364
1365
1366
1367
1368
1369
1370
1371
1372
1373
1374
1375
1376
1377
1378
1379
1370
1371
1372
1373
1374
1375
1376
1377
1378
1379
1380
1381
1382
1383
1384
1385
1386
1387
1388
1389
1380
1381
1382
1383
1384
1385
1386
1387
1388
1389
1390
1391
1392
1393
1394
1395
1396
1397
1398
1399
1390
1391
1392
1393
1394
1395
1396
1397
1398
1399
1400
1401
1402
1403
1404
1405
1406
1407
1408
1409
1400
1401
1402
1403
1404
1405
1406
1407
1408
1409
1410
1411
1412
1413
1414
1415
1416
1417
1418
1419
1410
1411
1412
1413
1414
1415
1416
1417
1418
1419
1420
1421
1422
1423
1424
1425
1426
1427
1428
1429
1420
1421
1422
1423
1424
1425
1426
1427
1428
1429
1430
1431
1432
1433
1434
1435
1436
1437
1438
1439
1430
1431
1432
1433
1434
1435
1436
1437
1438
1439
1440
1441
1442
1443
1444
1445
1446
1447
1448
1449
1440
1441
1442
1443
1444
1445
1446
1447
1448
1449
1450
1451
1452
1453
1454
1455
1456
1457
1458
1459
1450
1451
1452
1453
1454
1455
1456
1457
1458
1459
1460
1461
1462
1463
1464
1465
1466
1467
1468
1469
1460
1461
1462
1463
1464
1465
1466
1467
1468
1469
1470
1471
1472
1473
1474
1475
1476
1477
1478
1479
1480
1481
1482
1483
1484
1485
1486
1487
1488
1489
1490
1491
1492
1493
1494
1495
1496
1497
1498
1499
1500
1501
1502
1503
1504
1505
1506
1507
1508
1509
1500
1501
1502
1503
1504
1505
1506
1507
1508
1509
1510
1511
1512
1513
1514
1515
1516
1517
1518
1519
1510
1511
1512
1513
1514
1515
1516
1517
1518
1519
1520
1521
1522
1523
1524
1525
1526
1527
1528
1529
1520
1521
1522
1523
1524
1525
1526
1527
1528
1529
1530
1531
1532
1533
1534
1535
1536
1537
1538
1539
1530
1531
1532
1533
1534
1535
1536
1537
1538
1539
1540
1541
1542
1543
1544
1545
1546
1547
1548
1549
1540
1541
1542
1543
1544
1545
1546
1547
1548
1549
1550
1551
1552
1553
1554
1555
1556
1557
1558
1559
1550
1551
1552
1553
1554
1555
1556
1557
1558
1559
1560
1561
1562
1563
1564
1565
1566
1567
1568
1569
1560
1561
1562
1563
1564
1565
1566
1567
1568
1569
1570
1571
1572
1573
1574
1575
1576
1577
1578
1579
1570
1571
1572
1573
1574
1575
1576
1577
1578
1579
1580
1581
1582
1583
1584
1585
1586
1587
1588
1589
1580
1581
1582
1583
1584
1585
1586
1587
1588
1589
1590
1591
1592
1593
1594
1595
1596
1597
1598
1599
1590
1591
1592
1593
1594
1595
1596
1597
1598
1599
1600
1601
1602
1603
1604
1605
1606
1607
1608
1609
1600
1601
1602
1603
1604
1605
1606
1607
1608
1609
1610
1611
1612
1613
1614
1615
1616
1617
1618
1619
1610
1611
1612
1613
1614
1615
1616
1617
1618
1619
1620
1621
1622
1623
1624
1625
1626
1627
1628
1629
16

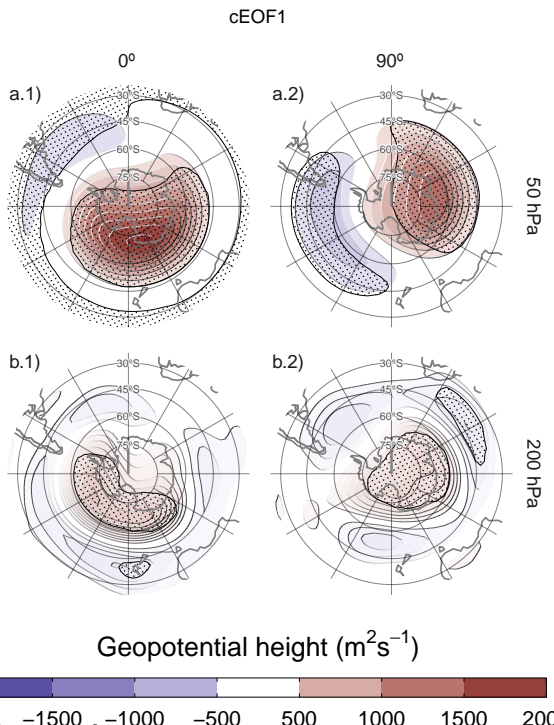


Fig. 4: Regression of SON geopotential height anomalies ($m^2 s^{-1}$) with the (column 1) 0° and (column 2) 90° phases of the first cEOF for the 1979 – 2019 period at (row a) 50 hPa and (row b) 200 hPa. These coefficients come from multiple linear regression involving the 0° and 90° phases. Areas marked with dots have p-values smaller than 0.01 adjusted for False Detection Rate.

associated with the 90° cEOF2. This monopole might indicate strengthening of the polar vortex associated with positive values of the 0° cEOF2 and weakening associated with negative values of 0° cEOF2. However, since these anomalies are not statistically significant, this feature should not be overinterpreted.

3.2.2 Temperature and Ozone

The signature of cEOFs variability on air temperature was also evaluated. Figure 6 shows regression maps of air temperature anomalies at 50 hPa and 200 hPa upon cEOF1. The distribution of temperature regression coefficients at 50 hPa and at 200 hPa mirror the geopotential height regression maps at 50 hPa (Fig. 4). In both levels, the 0° cEOF1 is associated with a positive centre over the South Pole with its centre moved slightly towards 150°E (Fig. 6 column 1). On the other hand, the regression maps on the 90° cEOF1 show a clearer wave 1 pattern with its maximum around 60°E .

Figure 7 shows the vertical distribution of the regression coefficients on cEOF1 from zonal anomalies of air temperature and of ozone mixing ratio

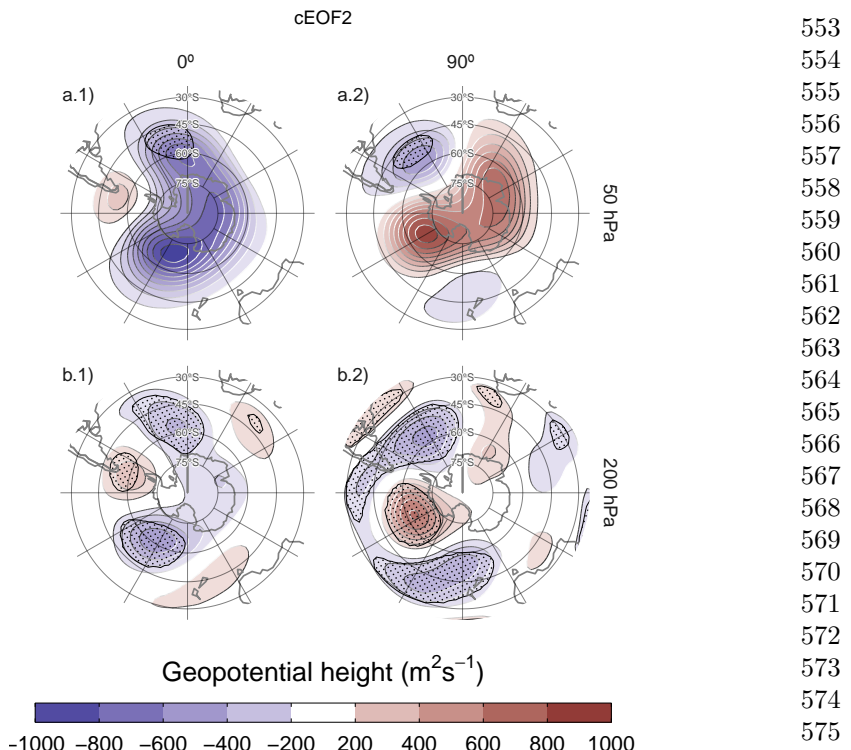


Fig. 5: Same as Figure 4 but for cEOF2.

averaged between 75°S and 45°S. Temperature zonal anomalies associated with cEOF1 show a clear wave 1 pattern for both 0° and 90° phases throughout the atmosphere above 250 hPa with a sign reversal above 10 hPa. As a result of the hydrostatic balance, this is the level in which the geopotential anomaly have maximum amplitude (not shown).

The maximum ozone regressed anomalies coincide with the minimum temperature anomalies above 10 hPa and with the maximum temperature anomalies below 10 hPa (Fig. 7). Therefore, the ozone zonal wave 1 is negatively correlated with the temperature zonal wave 1 in the upper stratosphere, and positively correlated in the upper stratosphere. This change in phase is observed in ozone anomalies forced by planetary waves that reach the stratosphere. In the photochemically-dominated upper stratosphere, cold temperatures inhibit the destruction of ozone, explaining the opposite behaviour for both variables as were elucidated with dynamical chemical models (Hartmann and Garcia, 1979; Wirth, 1993; Smith, 1995). On the other hand, in the advectively-dominated lower stratosphere, ozone anomalies are 1/4 wavelength out of phase with horizontal and vertical transport, which are in addition 1/4 wavelength out of phase with temperature anomalies, resulting in same sign

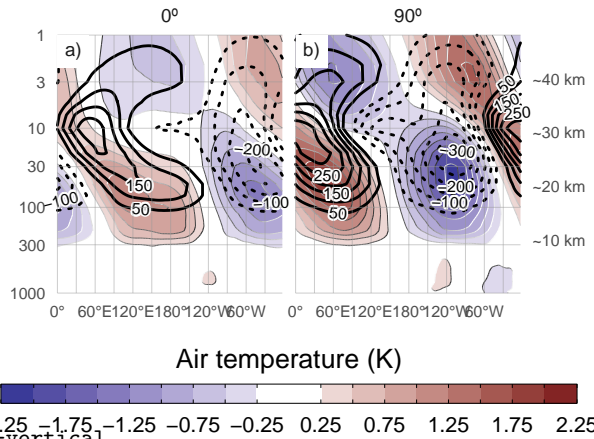
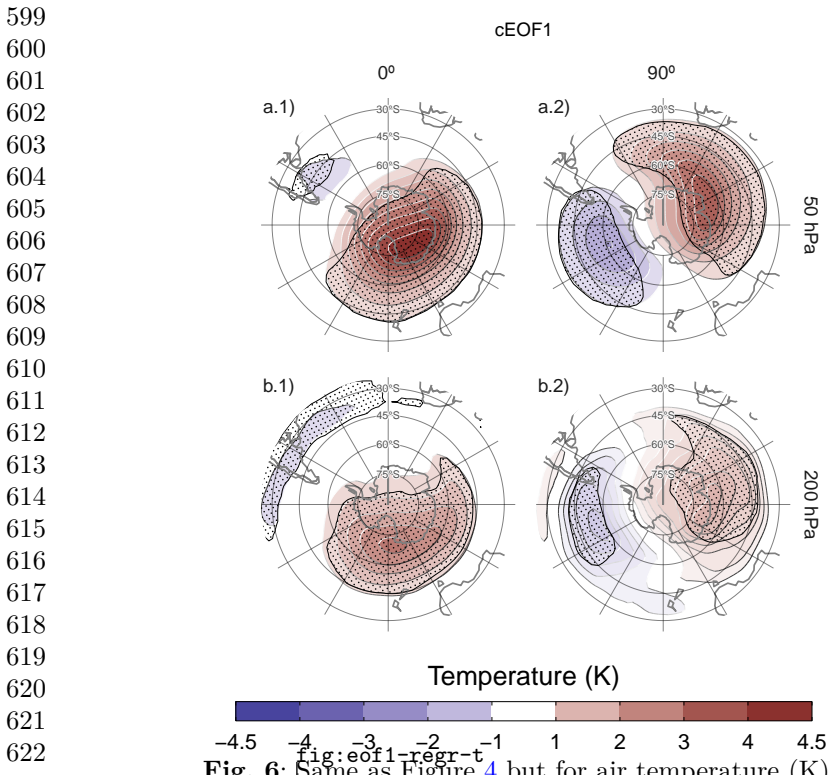


Fig. 7: Regression of SON zonal anomalies averaged between 75°S and 45°S of mean air temperature (shaded, Kelvin) and ozone mixing ratio (contours, negative contours with dashed lines, labels in parts per billion by mass) with the (a) 0° and (b) 90° phase of the cEOF1 for the 1979 – 2019 period.

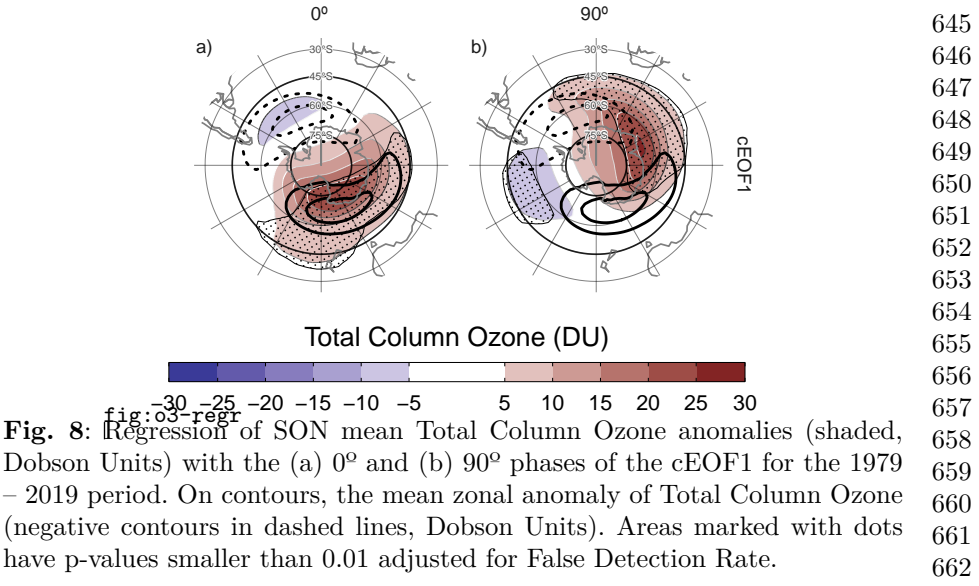


Table 2: Correlation coefficients (r) between cEOF2 components and the PSA1 and PSA2 modes computed as [Mo and Paegle \(2001\)](#) for the 1979 – 2019 period. 95% confidence intervals in parenthesis. p-values lower than 0.01 in bold.

PC	cEOF2	
	Real	Imaginary
PSA1	0.26 (CI: -0.04 – 0.52)	0.82 (CI: 0.69 – 0.9)
PSA2	0.79 (CI: 0.63 – 0.88)	-0.02 (CI: -0.32 – 0.29)

anomalies for the response of both variables ([Hartmann and Garcia, 1979](#); [Wirth, 1993](#); [Smith, 1995](#)).

The regression maps of TOC anomalies upon cEOF1 (Fig. 8) show zonal wave 1 patterns associated with both components of cEOF1. The climatological position of the springtime Ozone minimum (ozone hole) is outside the South Pole and towards the Weddell Sea (e.g. [Grytsai, 2011](#)). Thus, the 0° cEOF1 regression field (Figure 8a) coincides with the climatological position of the ozone hole, while it is 90° out of phase for the 90° cEOF1. The temporal correlation between the amplitudes of TOC planetary wave 1 and the amplitude of cEOF1 is 0.79 (CI: 0.63 – 0.88), while the correlation between their phases is -0.85 (CI: -0.92 – -0.74). Consequently, cEOF1 is strongly related with the SH ozone variability.

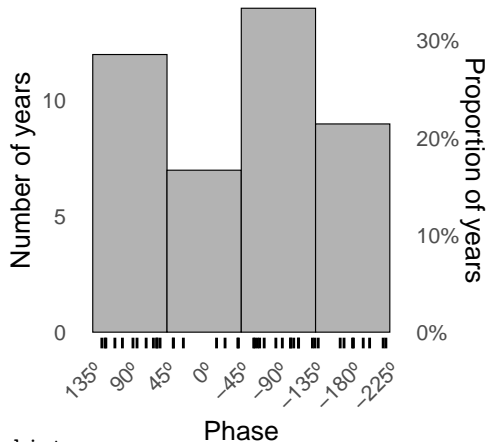


Fig. 9: `fig:phase-histogram` Histogram of phase distribution of cEOF2 phase for the 1979 – 2019 period. Bins are centred at 90°, 0°, -90°, -180° with a binwidth of 90°. The small vertical lines near the horizontal axis mark the observations.

3.3 PSA

Given the similarity between the cEOF2 related-associated structures (Fig. 5) and documented PSA patterns, we study the relationship between them. Table 2 shows the correlations between the two PSA indices and the time series for 0° and 90° phases of cEOF2. As visually anticipated by Figure 5, there is a large positive correlation between PSA1 and 90° cEOF2, and between PSA2 and 0° cEOF2. On the other hand, there is no significant relationship between PSA1 and 0° cEOF2, and between PSA2 and 90° cEOF2. As a result, cEOF2 represents well both the spatial structure and temporal evolution of the PSA modes, so it is possible to make an association between its two phases and the two PSA modes. That is, the phase election for cEOF2 that maximises the relationship between ENSO and 90° cEOF2, also maximises the association between cEOF2 components and PSA modes (not shown).

Figure 9 shows an histogram that counts the number of SON seasons in which the cEOF2 phase was close to each of the four particular phases (positive/negative of 0° and 90° phases), with the observations for each season marked as rugs on the horizontal axis. In 62% of seasons cEOF2 has a phase similar to either the negative or positive 90° phase, making the 90° phase the most common phase. This is also the phase that is most correlated with ENSO by the definition of the 0° phase as described in Section 2.

Therefore, by virtue of being the most common phase, the 90° cEOF2 explains more variance than the 0° cEOF2. Conventional EOF analysis will therefore tend to separate them relatively cleanly, with the EOF representing the 90° cEOF2 always leading the one representing the 0° cEOF2. This phase preference is in agreement with Irving and Simmonds (2016), who found a

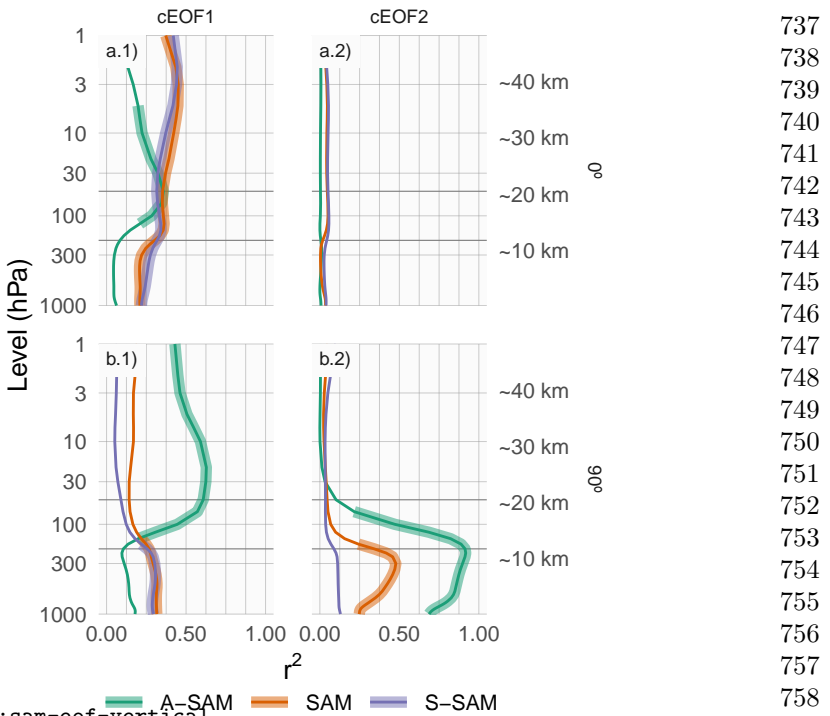


Fig. 10: Coefficient of determination (r^2) between each component of cEOFs and the SAM, Asymmetric SAM (A-SAM) and Symmetric SAM (S-SAM) indices computed at each level for the 1979 – 2019 period. Thick lines represent estimates with p -value < 0.01 corrected for False Detection Rate (Benjamini and Hochberg, 1995).

bimodal distribution to PSA-like variability (compare our Figure 9 with their Figure 6).

3.4 SAM

We now explore the relationship between SAM and the cEOFs motivated by the resemblance between cEOFs regression maps and SAM patterns shown in Section 3.2. We computed the coefficient of determination between the cEOFs time series and the three SAM indices (SAM, A-SAM and S-SAM) defined by Campitelli et al (2022b) at each vertical level (Fig. 10). The SAM index is statistically significantly correlated with the 0° cEOF1 in all levels, and with the 90° cEOF1 and 90° cEOF2 in the troposphere. On the other hand, correlations between SAM and the 0° cEOF2 are non-significant.

The relationship between the SAM and cEOF1 in the troposphere is explained entirely by the zonally symmetric component of the SAM as shown by the high correlation with the S-SAM below 100 hPa and the low and statistically non-significant correlations between the A-SAM and either the 0°

18 *SH zonally asymmetric circulation with cEOF*

783 or 90° cEOF1. In the stratosphere, the 0° cEOF1 is correlated with both A-
 784 SAM and S-SAM, while the 90° cEOF1 is highly correlated only with the
 785 A-SAM. These correlations are consistent with the regression maps of geopo-
 786 tential height in Figure 4 and their comparison with those obtained for SAM,
 787 A-SAM and S-SAM by [Campitelli et al \(2022b\)](#).

788 In the case of 90° cEOF2, its correlation with the SAM for the troposphere
 789 is associated to the asymmetric variability of the SAM. Indeed, the 90° cEOF2
 790 shares up to 92% variance with the A-SAM and only 12% at most with the
 791 S-SAM (Figure 10.b2). Such extremely high correlation between A-SAM and
 792 90° cEOF2 suggests that the modes obtained in this work are able to charac-
 793 terise the zonally asymmetric component of the SAM described previously by
 794 [Campitelli et al \(2022b\)](#).

795

796

3.5 Tropical sources of cEOFs variabitliy

797 The connections between cEOFs and tropical sources of variability were also
 798 assessed. Figure 11 shows the regression maps of Sea Surface Temperature
 799 (SST) and streamfunction anomalies at 200 hPa upon standardised cEOF2.
 800 As well as regression maps for the 0° and 90° phases, we include corresponding
 801 regressions for two intermediate directions (corresponding to 45° and 135°).

802 The 90° cEOF2 (second row) is associated with strong positive SST anom-
 803 alies on the Central to Eastern Pacific and negative anomalies over an area
 804 across northern Australia, New Zealand the South Pacific Convergence Zone
 805 (SPCZ) (Figure 11.b1). The regression field of SST anomalies bears a strong
 806 resemblance with canonically positive ENSO ([Bamston et al, 1997](#)). Indeed,
 807 there is a significant and very high correlation (0.76 (CI: 0.6 – 0.87)) between
 808 the ONI and the 90° cEOF2 time series. In addition to the Pacific ENSO-like
 809 pattern, there are also positive anomalies in the western Indian Ocean and
 810 negative values in the eastern Indian Ocean, resembling a positive IOD ([Saji
 811 et al, 1999](#)). Consistently, the correlation between the 90° cEOF2 and the DMI
 812 is 0.62 (CI: 0.38 – 0.78).

813 The 90° cEOF2 is associated with strong wave-like streamfunction anom-
 814 alies emanating from the tropics (Figure 11.b2), both from the Central Pacific
 815 sector and the Indian Ocean. The atmospheric response associated with 90°
 816 cEOF2 is then consistent with the combined effect of ENSO and the IOD on
 817 the extratropics: with SST anomalies inducing anomalous tropical convection
 818 that in turn excite Rossby waves propagating meridionally towards higher
 819 latitudes ([Mo, 2000; Cai et al, 2011a; Nuncio and Yuan, 2015](#)).

820 However, the cEOF2 is not associated with the same tropical SST anomaly
 821 patterns at all their phases Figure 11.d1 and d2 show that the 0° cEOF2 is
 822 not associated either with any significant SST nor streamfunction anomalies
 823 in the tropics. As a result, the correlation between the 0° cEOF2 and ENSO
 824 is not significant (0 (CI: -0.3 – 0.3)). Meanwhile, Rows a and c in Fig. 11 show
 825 that the intermediate phases are still associated with significant SST regressed
 826 anomalies over the Pacific Ocean, but at slightly different locations. The 135°
 827 phase is associated with SST anomalies in the central Pacific (Fig. 11a.1),
 828

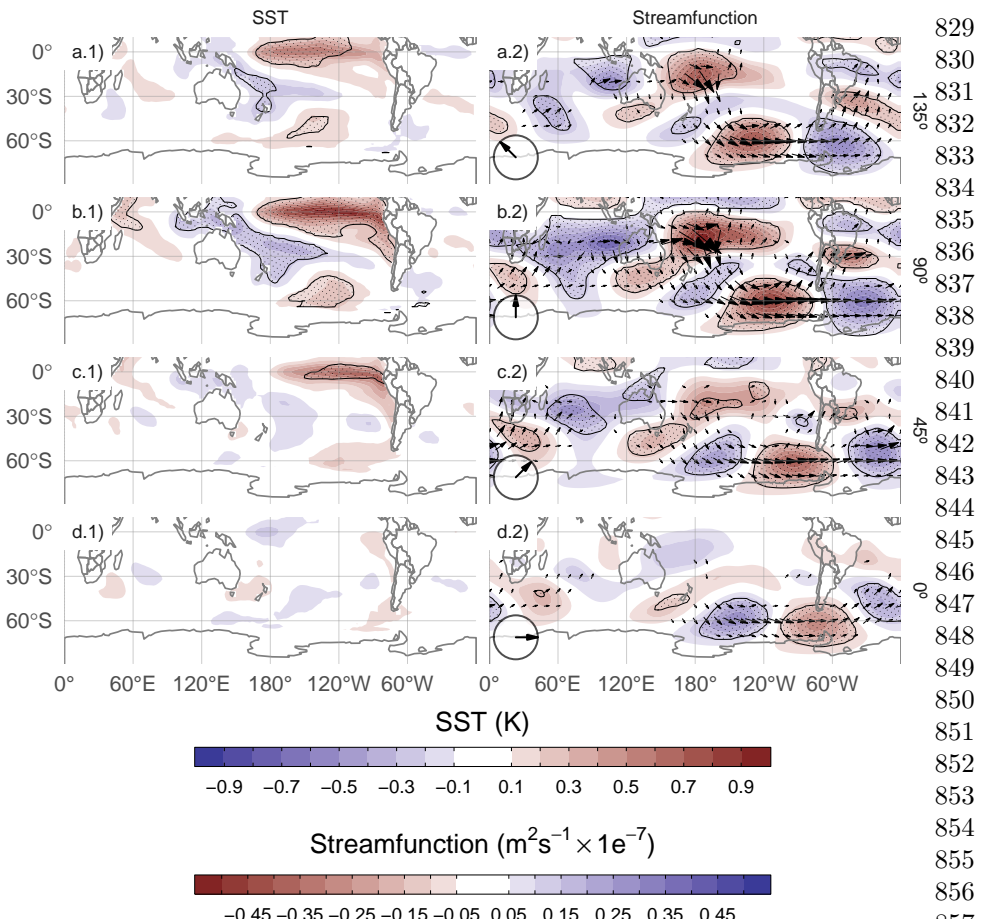


Fig. 11: Regression of SST (K, left column) and streamfunction zonal anomalies ($m^2/s \times 10^{-7}$, shaded) with their corresponding activity wave flux (vectors) (right column) upon cEOF2 different phases (illustrated in the lower-left arrow) for the 1979 – 2019 period. Areas marked with dots have p-values smaller than 0.01 adjusted for FDR.

fig:sst-psi-2

while the 45° phase is associated with SST anomalies that correspond roughly to the Central Pacific and Eastern Pacific “flavours” of ENSO, respectively (Fig. 11c.1) (Kao and Yu, 2009). Both phases are also associated to wave trains generated in the region surrounding Australia and propagates toward the extra-tropics, although less intense than the ones associated with the 90° phase.

To further explore the relationship between tropical forcing and phases of the cEOF2, Figure 12 shows the ONI plotted against the cEOF2 phase for each SON trimester between 1979 and 2019, highlighting years in which the magnitude of cEOF2 is above the median. In years with positive (negative)

829
830
831
832
833
834
835
836
837
838
839
840
841
842
843
844
845
846
847
848
849
850
851
852
853
854
855
856
857
858
859
860
861
862
863
864
865
866
867
868
869
870
871
872
873
874

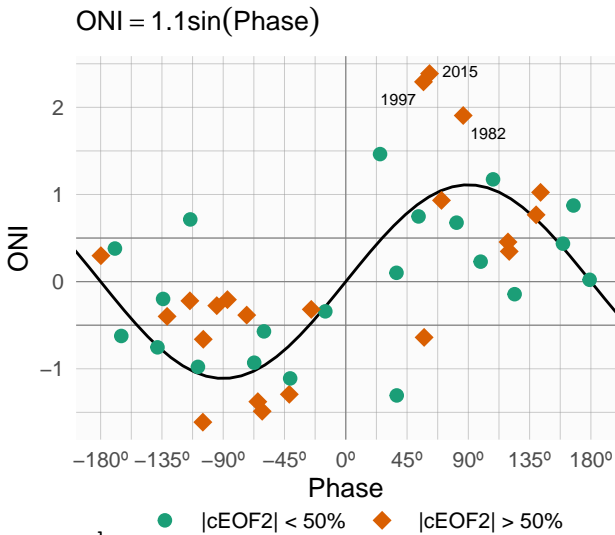


Fig. 12: fig:enso-phase SON ONI values plotted against cEOF2 phase for the 1979 – 2019 period. Years with magnitude of cEOF2 greater (smaller) than the 50th percentile are shown as orange diamonds (green circles). Black line is the fit $\text{ONI} \sim \sin(\text{phase})$ computed by weighted OLS using the magnitude of the cEOF2 as weights.

ONI, the cEOF2 phase is mostly around 90° (-90°). In the neutral ENSO seasons, the cEOF2 phase is much more variable. The black line in Figure 12 is a sinusoidal fit of the relationship between ONI and cEOF2 phase. The r^2 corresponding to the fit is 0.57, statistically significant with p-value < 0.001 , indicating a quasi-sinusoidal relation between these two variables.

The correlation between the absolute magnitude of the ONI and the cEOF2 amplitude is 0.45 (CI: 0.17 – 0.66). However, this relationship is mostly driven by the three years with strongest ENSO events in the period (2015, 1997, and 1982) which coincide with the three years with strongest cEOF2 magnitude (not shown). If those years are removed, the correlation becomes non-significant (0.04 (CI: -0.28 – 0.35)). Furthermore, even when using all years, the Spearman correlation –which is robust to outliers– is also non-significant (0.2, p-value = 0.21). Therefore, although the location of tropical SST anomalies seem to have an effect in defining the phase of the cEOF2, the relationship between the magnitude of cEOF2 and ONI remains uncertain and might be only evident in very strong ENSO events, that are scarce in the historical observational record.

We conclude that the wave train represented by cEOF2 can be both part of the internal variability of the extratropical atmosphere and forced by tropical SSTs. In the former case, the wave train has little phase preference. However, when cEOF2 is excited by tropical SST variability, it tends to remain locked to

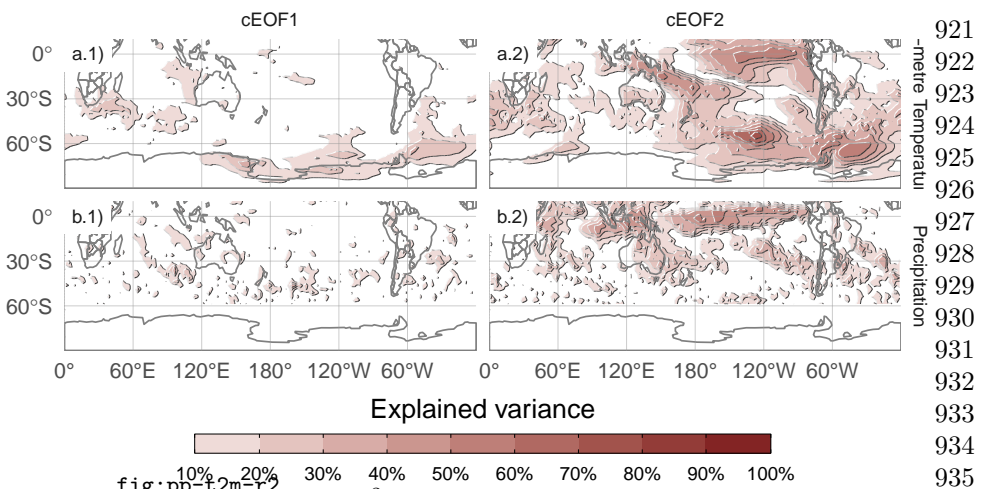


Fig. 13: Explained variance (r^2 as percentage) of 2-metre temperature (row a) and precipitation (row b) anomalies by the regression upon cEOF1 (column 1) and cEOF2 (column 2).

the 90° phase. This explains the relative over-abundance of years with cEOF2 near positive and negative 90° phase in Figure 9.

Unlike the cEOF2 case, there are no significant SST regressed anomalies associated with either the 0° or 90° cEOF1 (Sup. Figure A.1). Consistently, streamfunction anomalies do not show any tropical influence. Instead, the 0° and 90° cEOF1 are associated with zonally propagating wave activity fluxes in the extra-tropics around 60°S , except for an equatorward flow from the coast of Antarctica around 150°E in the 0° phase. This suggests that the variability of cEOF1 is driven primary by the internal variability of the extra-tropics.

3.6 cEOFs surface impacts

The influence of cEOFs variability in the anomalies of both 2-metre air temperature and precipitation in the SH was also explored. Figure 13 shows the 2-meter temperature and precipitation anomalies explained variance by the multiple linear model of both 0° and 90° cEOF1 (column 1), and both 0° and 90° cEOF2 (column 2). The variance explained by cEOF1 for precipitation anomalies and temperature anomalies in most regions is extremely low, except for the northern tip of the Antarctic Peninsula, northern Weddell Sea and the Ross Sea coast (Fig. 13a.1).

This lack of strong relationship between the cEOF1 and SST, temperature and precipitation might be surprising considering the correlation between the cEOF1 and the SAM (Fig. 10 column 1) and the correlation between SAM and Central Pacific SST, temperature east and west of the Antarctic Peninsula, and with precipitation in western Australia (Fogt and Marshall, 2020). There are two main reasons for this. First, the correlation between cEOF1

precipitation

921
922
923
924
925
926
927
928
929
930
931
932
933
934
935
936
937
938
939
940
941
942
943
944
945
946
947
948
949
950
951
952
953
954
955
956
957
958
959
960
961
962
963
964
965
966

22 *SH zonally asymmetric circulation with cEOF*

967 and the SAM in the troposphere is modest, with less than 50% of shared variance
 968 (Fig. 10 column 1), so these indices are not expected to be equivalent.
 969 Second, Campitelli et al (2022b) showed that the strong relationship between
 970 the SAM and Pacific SSTs and temperature anomalies around the Antarctic
 971 Peninsula is mainly due to the asymmetric part of the SAM. Meanwhile, the
 972 cEOF1 is significantly correlated only with the symmetric part of the SAM
 973 (Fig. 10 column 1), which by itself is not significantly correlated with surface
 974 temperatures in that area.

975 On the other hand, the cEOF2 explained variance is greater than 50% in
 976 some regions for both variables (Fig. 13 column 2). For 2-metre temperature,
 977 there are high values in the tropical Pacific and the SPCZ, as well as the
 978 region following an arc between New Zealand and the South Atlantic, with
 979 higher values in the Southern Ocean. Over the continents, there are moderate
 980 values of about 30% variance explained in southern Australia, Southern South
 981 America and the Antarctic Peninsula. For precipitation, there are high values
 982 over the tropics. At higher latitudes, moderate values are observed over eastern
 983 Australia and some regions of southern South America.

984 Since the cEOF1 has a relatively weak signal in the surface variables
 985 explored here, we will only focus on the cEOF2 influence. Figure 14 shows
 986 regression maps of 2-metre temperature (column 1) and precipitation (column
 987 2) anomalies upon different phases of standardised cEOF2.

988 Temperature anomalies associated with the 90° cEOF (Fig. 14.b1) show
 989 positive values in the tropical Pacific, consistent with SSTs anomalies associ-
 990 ated with the same phase (Fig. 11.b1). At higher latitudes there is a wave-like
 991 pattern of positive and negative values that coincide with the nodes of the
 992 850 hPa geopotential height regression patterns. This is consistent with tem-
 993 perature anomalies produced by meridional advection of temperature by the
 994 meridional winds arising from geostrophic balance. Over the continents, the
 995 90° cEOF2 (Fig. 14b.1) is associated with positive regressed temperature
 996 anomalies in southern Australia and negative regressed anomalies in south-
 997 ern South America and the Antarctic Peninsula, that are a result of the wave
 998 train described before.

999 The temperatures anomalies associated with the 0° cEOF2 (Fig. 14d.1)
 1000 are less extensive and restricted to mid and high latitudes.

1001 Over the continents, the temperature anomalies regressions are non significant,
 1002 except for positive anomalies near the Antarctic Peninsula.

1003 Tropical precipitation anomalies associated with the 90° cEOF2 are strong,
 1004 with positive anomalies in the central Pacific and western Indian, and negative
 1005 anomalies in the eastern Pacific (Fig. 14b.2). This field is consistent with
 1006 the SST regression map (Fig. 14b.1) as the positive SST anomalies enhance
 1007 tropical convection and the negative SST anomalies inhibits it.

1008 In the extra-tropics, the positive 90° cEOF2 is related to drier conditions
 1009 over eastern Australia and the surrounding ocean, that it is similar signal as
 1010 the one associated with ENSO (Cai et al, 2011a). However, the 90° cEOF2
 1011 is not the phase most correlated with precipitation in that area. The 135°
 1012

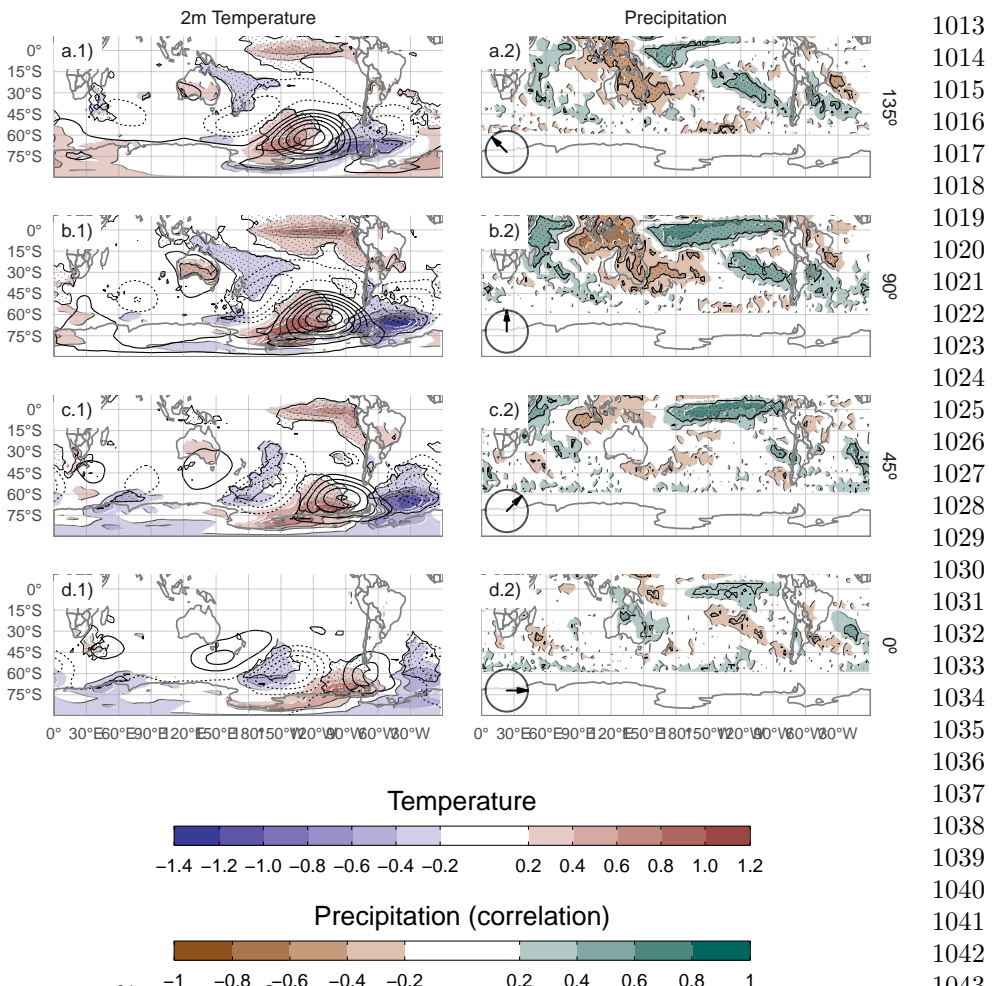


Fig. 14: `fig:pp-temp-2`: Regression of SON mean 2-meter temperature (K, shaded) and 850 hPa geopotential height (m, contours) (column 1), and precipitation (correlation, column 2) upon different phases of cEOF2. For the 1979 – 2019. Areas marked with dots have p-values smaller than 0.01 adjusted for False Detection Rate.

phase (an intermediate between positive 90° and 180° cEOF2) component is associated with stronger and more extensive temporal correlations with precipitation over Australia and New Zealand. The influence of cEOF2 in Australian precipitation could be more related to the direct impacts of SST anomalies in the surrounded oceans rather than on the interconnection pattern represented by the cEOF2.

Over South America, the 90° cEOF2 has positive correlations with precipitation in South Eastern South America (SESA) and central Chile, and negative

1059 correlations in eastern Brazil. This correlation field matches the springtime
 1060 precipitation signature of ENSO (e.g. Cai et al., 2020) and it is also similar
 1061 to the precipitation anomalies associated with the A-SAM (Campitelli et al.,
 1062 2022b). This result is not surprising considering the close relationship of the
 1063 90° cEOF2 with both ONI and A-SAM index, which was shown previously.
 1064 Furthermore, it consolidates the identification of the cEOF2 with the PSA
 1065 pattern. Resembling the relationship between ONI and the phase of cEOF2
 1066 (Fig. 12), there is a cEOF2 phase dependence of the precipitation anomalies
 1067 in SESA (not shown).

1068 The correlation coefficients between precipitation anomalies and the 0°
 1069 cEOF2 (Fig. 14d.2) are weaker than for 90° cEOF2. There is a residual pos-
 1070 itive correlation in the equatorial eastern Pacific and small, not statistically
 1071 significant positive correlations over eastern Australia and negative ones over
 1072 New Zealand.

1073

1074 4 Discussion and conclusions

1075

discussion

1076 In this study we assessed extratropical Southern Hemisphere zonally asym-
 1077 metric circulation in austral spring. For this purpose, we derived two complex
 1078 indices using Complex Empirical Orthogonal Functions and used to charac-
 1079 terise both amplitude and phase of planetary waves.

1080 The cEOF1 represents the variability of the zonal wave 1 in the strato-
 1081 sphere and is closely related to stratospheric variability such as anomalies in
 1082 Total Column Ozone. Otherwise, this complex EOF is not related with SST
 1083 variability and continental precipitation in the Southern Hemisphere. On the
 1084 other hand, the cEOF2 represents a wave-3 pattern with maximum magnitude
 1085 in the Pacific sector, that is an alternative representation of the PSA1 and
 1086 PSA2 patterns (Mo and Paegle 2001). The 90° cEOF2 can be identified with
 1087 the PSA1 and the 0° cEOF2 with the PSA2. While the cEOF2 variability is
 1088 related to surface impacts, the cEOF1 surface influence is almost negligible.
 1089 For instance, precipitation anomalies in South America associated with the
 1090 90° cEOF2 show a clear ENSO-like impact, with positive anomalies in South-
 1091 eastern South America, negative anomalies in Southern Brazil and positive
 1092 anomalies in central Chile for positive 90° cEOF2 phase.

1093 Variability patterns that arise from cEOF methodology describe the zon-
 1094 ally asymmetric springtime extratropical SH circulation, reproducing previous
 1095 features such as the variability related to PSAs or A-SAM.

1096 Since the spatial fields obtained from both components of cEOF2, which
 1097 resemble PSA patterns, are in quadrature by construction, the cEOF method-
 1098 ology allows to derive, for the first time to our knowledge, a joint PSA
 1099 index from the resulted amplitude and phase. These patterns are not forced
 1100 to be orthogonal to other modes of circulation, like they are in standard
 1101 EOF methodology. This allows us to show for example, that the 90° cEOF2,
 1102 corresponding to PSA1 variability, is closely associated to the SAM in the
 1103 troposphere. Previous research in the SAM-PSA relationship had the issue
 1104

that the SAM and the PSA patterns are not independently derived and so the correlation between these indices had to be zero by construction. 1105
 Most studies on the relationship between ENSO and SAM rely on correlations 1106
 between an ENSO index and the SAM index (e.g. L'Heureux and 1107
 Thompson, 2006, Cai et al (2011b)) or between the SAM index and other 1108
 variables associated with tropical convection, such as OLR or tropical SSTS 1109
 (e.g. Carvalho et al, 2005). However, Campitelli et al (2022b) showed that the 1110
 correlation between ENSO and SAM is almost completely explained by the 1111
 asymmetric component of the SAM. In this work we show that the asymmetric 1112
 component of the SAM can be identified with the PSA1. Therefore, the 1113
 correlation between ENSO and SAM is predominantly the correlation between 1114
 ENSO and PSA1. This sheds new light into the previous literature, as it cannot 1115
 be assumed that a high correlation between ENSO and SAM indexes indicates 1116
 a relationship between ENSO and zonally symmetric variability. 1117
 1118

Further investigation is necessary to determine the connection between 1119
 the symmetric component of the SAM and the PSA. It is possible that the 1120
 PSA may force a zonally symmetric response (or vice versa) via wave-zonal 1121
 mean flow interactions, or that this correlation is simply a statistical artefact 1122
 resulting from the EOF methodology used to define the SAM and the fact 1123
 that the spatial structure of the PSA projects onto the spatial structure of the 1124
 symmetric SAM. 1125

Irving and Simmonds (2016) argued that there is some disagreement in the 1126
 literature of whether the phase of the PSA pattern is affected by the location 1127
 of tropical SST anomalies. With the methodology used in this study, we were 1128
 able to show not only that the cEOF2 tends to be in the positive or negative 1129
 90° phase (~PSA1) when the ENSO region is warm or cold, respectively, but 1130
 also that central Pacific SST anomalies tend to align the cEOF towards the 1131
 negative 0° phase and eastern Pacific SST anomalies tend to align it towards 1132
 positive 0° phase. When ENSO phase is neutral, the cEOF2 is still as active, 1133
 but with no preferred phase. The latter agrees with the results of Cai and 1134
 Watterson (2002), who showed that the CSIRO Model can develop PSA-like 1135
 variability even in the absence of ENSO forcing (i.e. with a climatological 1136
 run), but that the variability of one of the PSA modes was enhanced when 1137
 adding the ENSO signal. The sensitivity of the phase of the PSAs to the 1138
 location of the tropical SST anomalies was also seen by Ciasto et al (2015), 1139
 who detected similar Rossby wave patterns associated with central Pacific and 1140
 eastern Pacific SST anomalies but with a change in phase. 1141

The method used in this study has similarities to the one used by Goyal 1142
 et al (2022) as they construct an index of amplitude and phase of zonal 1143
 wave 3-like variability by combining the two leading EOFs of meridional wind 1144
 anomalies. The patterns obtained by them bear high resemblance with cEOF2. 1145
 Although a detailed comparison is out of scope for this paper, the cEOF analysis 1146
 has the advantage of constructing the indices based on patterns that are 1147
 exactly in quadrature by construction. 1148
 1149
 1150

1151 The methodology proposed in this study allows for a deeper understanding
 1152 of the zonally asymmetric springtime extratropical SH circulation such as a
 1153 better description of PSA like variability using a unique complex index and the
 1154 understanding of relationship between PSAs and ENSO or SAM variability.
 1155 Further work should extend this analysis to other seasons and further study
 1156 the relationship between the cEOF2 and the SAM.

1157

1158 **Declarations**

1159

declarations

1160 **Funding**

1161

funding

1162 The research was supported by UBACyT20020170100428BA, Consejo
 1163 Nacional de Investigaciones Científicas y Técnicas (CONICET) PIP
 1164 11220200102038CO, PICT-2020-SERIEA-I-INVI-00540, and the CLIMAX
 1165 Project funded by Belmont Forum/ANR-15-JCL/-0002-01. Elio Campitelli
 1166 was supported by a PhD grant from CONICET, Argentina.

1167

1168 **Conflict of interest/Competing interests**

1169

conflict-of-interestcompeting-interests

1170 The authors have no relevant financial or non-financial interests to disclose.

1170

1171 **Ethics approval**

1172

ethics-approval

1173 Not applicable.

1174

1175 **Consent to participate**

1176

consent-to-participate

1177 Not applicable.

1178

1179 **Consent for publication**

1180

consent-for-publication

1181 Not applicable.

1182

Availability of data and materials

1183

availability-of-data-and-materials

1184 All data used in this paper available in a Zenodo repository ([Campitelli et al,](#)
 1185 [2022a](#)) (<https://zenodo.org/record/6612429>). Indices updated monthly and
 1186 daily will be made available at [http://www.cima.fcen.uba.ar/~elio.campitelli/
 1187 shceof/](http://www.cima.fcen.uba.ar/~elio.campitelli/shceof/).

1188

It is also freely available from their respective sources:

1189

- ERA5 data can be obtained via the Copernicus Climate Data Store (<https://cds.climate.copernicus.eu/cdsapp#!/dataset/reanalysis-era5-pressure-levels-monthly-means/>).
- ERSSSTv5 can be obtained via NOAA's NCEI website at [https://www.ncei.noaa.gov/access/metadata/landing-page/bin/iso?id=gov.noaa.ncdc:
 1193 C00927](https://www.ncei.noaa.gov/access/metadata/landing-page/bin/iso?id=gov.noaa.ncdc:C00927)

1194

1195

1196

- CMAP Precipitation data provided by the NOAA/OAR/ESRL PSL, Boulder, Colorado, USA, from their Web site at <https://psl.noaa.gov/data/gridded/data.cmap.html>. 1197
1198
1199
- The Oceanic Niño Index is available via NOAA's Climate Prediction Center: https://www.cpc.ncep.noaa.gov/products/analysis_monitoring/ensostuff/detrend.nino34.ascii.txt. 1200
1201
1202
- The Oceanic Niño Index is available via NOAA's Climate Prediction Center: https://www.cpc.ncep.noaa.gov/products/analysis_monitoring/ensostuff/detrend.nino34.ascii.txt. 1203
1204
1205
- The Dipole Mode Index is available via Global Climate Observing System Working Group on Surface Pressure: https://psl.noaa.gov/gcos_wgsp/Timeseries/Data/dmi.had.long.data 1206
1207
1208
1209

Code availability

A version-controlled repository of the code used to create this analysis, including the code used to download the data can be found at <https://github.com/eliocamp/shceof>.

Authors' contributions

E.C. made the data curation, formal analysis and prepared all the figures. E.C. and L.D. wrote the main manuscript text. All authors reviewed the manuscript.

A Extra figures

code-availability
1211
1212
1213
1214
1215
1216
1217
1218
1219
1220
1221
1222
1223
1224
1225
1226
1227
1228
1229
1230
1231
1232
1233
1234
1235
1236
1237
1238
1239
1240
1241
1242

authors-contributions

extra-figures

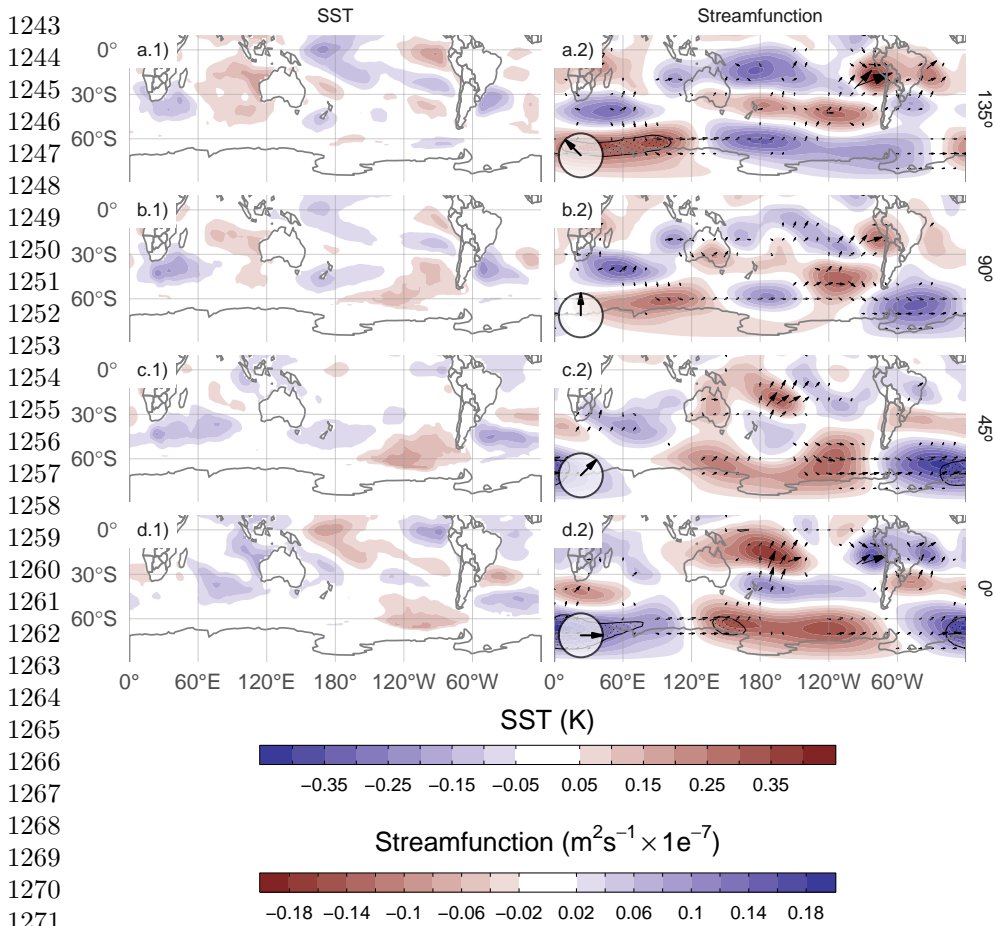


Fig. A.1: Same as Figure 11 but for cEOF1.

fig:sst-psi-1

References

- Adams JC, Swartztrauber PN, Sweet R (1999) FISHPACK, a package of Fortran subprograms for the solution of separable elliptic partial differential equations. <https://www2.cisl.ucar.edu/resources/legacy/fishpack>
- Albers S, Campitelli E (2020) Rsoi: Import Various Northern and Southern Hemisphere Climate Indices
- Allaire JJ, Xie [aut Y, cre, et al (2020) Rmarkdown: Dynamic Documents for R
- Baldwin MP, Thompson DWJ (2009) A critical comparison of stratosphere–troposphere coupling indices. Quarterly Journal of the Royal Meteorological Society 135(644):1661–1672. <https://doi.org/10.1002/qj.479>

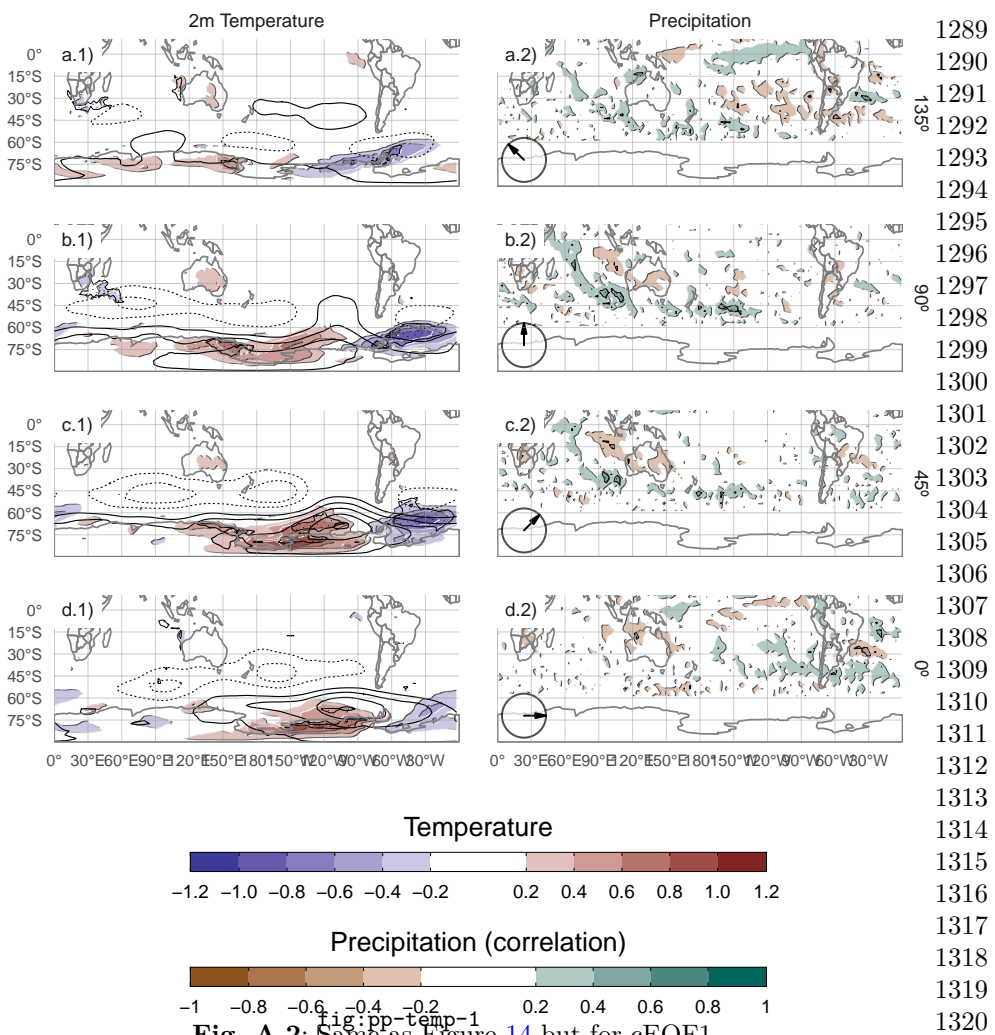


Fig. A.2: Same as Figure 14 but for cEOF1.

Bamston AG, Chelliah M, Goldenberg SB (1997) Documentation of a highly ENSO-related sst region in the equatorial pacific: Research note. *Atmosphere-Ocean* 35(3):367–383. <https://doi.org/10.1080/07055900.1997.9649597>

Bell B, Hersbach H, Berrisford P, et al (2020) ERA5 monthly averaged data on pressure levels from 1950 to 1978 (preliminary version). Copernicus Climate Change Service (C3S) Climate Data Store (CDS) (Accessed on <26-08-2021>), <https://cds.climate.copernicus.eu/cdsapp#!/dataset/reanalysis-era5-pressure-levels-monthly-means-preliminary-back-extension?tab=overview>

1289
1290
1291
1292
1293
1294
1295
1296
1297
1298
1299
1300
1301
1302
1303
1304
1305
1306
1307
1308
1309
1310
1311
1312
1313
1314
1315
1316
1317
1318
1319
1320
1321
1322
1323
1324
1325
1326
1327
1328
1329
1330
1331
1332
1333
1334

- 1335 Benjamini Y, Hochberg Y (1995) Controlling the False Discovery Rate: A
1336 Practical and Powerful Approach to Multiple Testing. *Journal of the Royal
1337 Statistical Society: Series B (Methodological)* 57(1):289–300. <https://doi.org/10.1111/j.2517-6161.1995.tb02031.x>
- 1339
- 1340 Cai W, Watterson IG (2002) Modes of Interannual Variability of the Southern
1341 Hemisphere Circulation Simulated by the CSIRO Climate Model. *Journal
1342 of Climate* 15(10):1159–1174. [https://doi.org/10.1175/1520-0442\(2002\)
015<1159:MOIVOT>2.0.CO;2](https://doi.org/10.1175/1520-0442(2002)
015<1159:MOIVOT>2.0.CO;2)
- 1344
- 1345 Cai W, van Rensch P, Cowan T, et al (2011a) Teleconnection Pathways
1346 of ENSO and the IOD and the Mechanisms for Impacts on Australian
1347 Rainfall. *Journal of Climate* 24(15):3910–3923. [https://doi.org/10.1175/
2011JCLI4129.1](https://doi.org/10.1175/
2011JCLI4129.1)
- 1349
- 1350 Cai W, Sullivan A, Cowan T (2011b) Interactions of ENSO, the IOD, and
1351 the SAM in CMIP3 Models. *Journal of Climate* 24(6):1688–1704. <https://doi.org/10.1175/2010JCLI3744.1>
- 1352
- 1353 Cai W, McPhaden MJ, Grimm AM, et al (2020) Climate impacts of the
1354 El Niño–Southern Oscillation on South America. *Nature Reviews Earth &
1355 Environment* 1(4):215–231. <https://doi.org/10.1038/s43017-020-0040-3>
- 1356
- 1357 Campitelli E (2020) metR: Tools for Easier Analysis of Meteorological Fields
1358
- 1359 Campitelli E, Díaz L, Vera C (2022a) Data for "Revisiting the Austral Spring
1360 Extratropical Southern Hemisphere zonally asymmetric circulation using
1361 complex Empirical Orthogonal Functions". [https://doi.org/10.5281/zenodo.
6612324](https://doi.org/10.5281/zenodo.
6612324)
- 1363
- 1364 Campitelli E, Díaz LB, Vera C (2022b) Assessment of zonally symmetric
1365 and asymmetric components of the Southern Annular Mode using a
1366 novel approach. *Climate Dynamics* 58(1):161–178. [https://doi.org/10.1007/
s00382-021-05896-5](https://doi.org/10.1007/
s00382-021-05896-5)
- 1368
- 1369 Carvalho LMV, Jones C, Ambrizzi T (2005) Opposite Phases of the Antarctic
1370 Oscillation and Relationships with Intraseasonal to Interannual Activity in
1371 the Tropics during the Austral Summer. *Journal of Climate* 18(5):702–718.
1372 <https://doi.org/10.1175/JCLI-3284.1>
- 1373
- 1374 Cazes-Boezio G, Robertson AW, Mechoso CR (2003) Seasonal Dependence of
1375 ENSO Teleconnections over South America and Relationships with Precipi-
1376 tation in Uruguay. *Journal of Climate* 16(8):1159–1176. [https://doi.org/10.
1175/1520-0442\(2003\)16<1159:SDOETO>2.0.CO;2](https://doi.org/10.
1175/1520-0442(2003)16<1159:SDOETO>2.0.CO;2)
- 1377
- 1378 Ciasto LM, Simpkins GR, England MH (2015) Teleconnections between Tropi-
1379 cal Pacific SST Anomalies and Extratropical Southern Hemisphere Climate.
1380

- Journal of Climate 28(1):56–65. <https://doi.org/10.1175/JCLI-D-14-00438.1> 1381
 1382
 1383
 1384
 1385
 1386
 1387
 1388
 1389
 1390
 1391
 1392
 1393
 1394
 1395
 1396
 1397
 1398
 1399
 1400
 1401
 1402
 1403
 1404
 1405
 1406
 1407
 1408
 1409
 1410
 1411
 1412
 1413
 1414
 1415
 1416
 1417
 1418
 1419
 1420
 1421
 1422
 1423
 1424
 1425
 1426
- Dowle M, Srinivasan A (2020) Data.table: Extension of 'data.frame' 1384
- Fogt RL, Marshall GJ (2020) The Southern Annular Mode: Variability, trends, and climate impacts across the Southern Hemisphere. WIREs Climate Change 11(4):e652. <https://doi.org/10.1002/wcc.652> 1385
 1386
 1387
 1388
 1389
 1390
 1391
 1392
 1393
 1394
 1395
 1396
 1397
 1398
 1399
 1400
 1401
 1402
 1403
 1404
 1405
 1406
 1407
 1408
 1409
 1410
 1411
 1412
 1413
 1414
 1415
 1416
 1417
 1418
 1419
 1420
 1421
 1422
 1423
 1424
 1425
 1426
- Gelbrecht M, Boers N, Kurths J (2018) Phase coherence between precipitation in South America and Rossby waves. Science Advances 4(12):eaau3191. <https://doi.org/10.1126/sciadv.aau3191> 1389
 1390
 1391
 1392
 1393
 1394
 1395
 1396
 1397
 1398
 1399
 1400
 1401
 1402
 1403
 1404
 1405
 1406
 1407
 1408
 1409
 1410
 1411
 1412
 1413
 1414
 1415
 1416
 1417
 1418
 1419
 1420
 1421
 1422
 1423
 1424
 1425
 1426
- Gong D, Wang S (1999) Definition of Antarctic Oscillation index. Geophysical Research Letters 26(4):459–462. <https://doi.org/10.1029/1999GL900003> 1389
 1390
 1391
 1392
 1393
 1394
 1395
 1396
 1397
 1398
 1399
 1400
 1401
 1402
 1403
 1404
 1405
 1406
 1407
 1408
 1409
 1410
 1411
 1412
 1413
 1414
 1415
 1416
 1417
 1418
 1419
 1420
 1421
 1422
 1423
 1424
 1425
 1426
- Goyal R, Jucker M, Gupta AS, et al (2022) A new zonal wave 3 index for the Southern Hemisphere. Journal of Climate -1(aop):1–25 1389
 1390
 1391
 1392
 1393
 1394
 1395
 1396
 1397
 1398
 1399
 1400
 1401
 1402
 1403
 1404
 1405
 1406
 1407
 1408
 1409
 1410
 1411
 1412
 1413
 1414
 1415
 1416
 1417
 1418
 1419
 1420
 1421
 1422
 1423
 1424
 1425
 1426
- Grytsai A (2011) Planetary wave peculiarities in Antarctic ozone distribution during 1979–2008. International Journal of Remote Sensing 32(11):3139–3151. <https://doi.org/10.1080/01431161.2010.541518> 1389
 1390
 1391
 1392
 1393
 1394
 1395
 1396
 1397
 1398
 1399
 1400
 1401
 1402
 1403
 1404
 1405
 1406
 1407
 1408
 1409
 1410
 1411
 1412
 1413
 1414
 1415
 1416
 1417
 1418
 1419
 1420
 1421
 1422
 1423
 1424
 1425
 1426
- Hartmann DL, Garcia RR (1979) A Mechanistic Model of Ozone Transport by Planetary Waves in the Stratosphere. Journal of the Atmospheric Sciences 36(2):350–364. [https://doi.org/10.1175/1520-0469\(1979\)036<0350:AMMOOT>2.0.CO;2](https://doi.org/10.1175/1520-0469(1979)036<0350:AMMOOT>2.0.CO;2) 1389
 1390
 1391
 1392
 1393
 1394
 1395
 1396
 1397
 1398
 1399
 1400
 1401
 1402
 1403
 1404
 1405
 1406
 1407
 1408
 1409
 1410
 1411
 1412
 1413
 1414
 1415
 1416
 1417
 1418
 1419
 1420
 1421
 1422
 1423
 1424
 1425
 1426
- Hersbach H, Bell B, Berrisford P, et al (2019) ERA5 monthly averaged data on pressure levels from 1979 to present. Copernicus Climate Change Service (C3S) Climate Data Store (CDS) (Accessed on <07-09-2021>). <https://doi.org/10.24381/cds.6860a573> 1389
 1390
 1391
 1392
 1393
 1394
 1395
 1396
 1397
 1398
 1399
 1400
 1401
 1402
 1403
 1404
 1405
 1406
 1407
 1408
 1409
 1410
 1411
 1412
 1413
 1414
 1415
 1416
 1417
 1418
 1419
 1420
 1421
 1422
 1423
 1424
 1425
 1426
- Hobbs WR, Raphael MN (2010) Characterizing the zonally asymmetric component of the SH circulation. Climate Dynamics 35(5):859–873. <https://doi.org/10.1007/s00382-009-0663-z> 1389
 1390
 1391
 1392
 1393
 1394
 1395
 1396
 1397
 1398
 1399
 1400
 1401
 1402
 1403
 1404
 1405
 1406
 1407
 1408
 1409
 1410
 1411
 1412
 1413
 1414
 1415
 1416
 1417
 1418
 1419
 1420
 1421
 1422
 1423
 1424
 1425
 1426
- Horel JD (1984) Complex Principal Component Analysis: Theory and Examples. Journal of Applied Meteorology and Climatology 23(12):1660–1673. [https://doi.org/10.1175/1520-0450\(1984\)023<1660:CPCATA>2.0.CO;2](https://doi.org/10.1175/1520-0450(1984)023<1660:CPCATA>2.0.CO;2) 1389
 1390
 1391
 1392
 1393
 1394
 1395
 1396
 1397
 1398
 1399
 1400
 1401
 1402
 1403
 1404
 1405
 1406
 1407
 1408
 1409
 1410
 1411
 1412
 1413
 1414
 1415
 1416
 1417
 1418
 1419
 1420
 1421
 1422
 1423
 1424
 1425
 1426
- Hoskins BJ, Hodges KI (2005) A New Perspective on Southern Hemisphere Storm Tracks. Journal of Climate 18(20):4108–4129. <https://doi.org/10.1175/JCLI3570.1> 1389
 1390
 1391
 1392
 1393
 1394
 1395
 1396
 1397
 1398
 1399
 1400
 1401
 1402
 1403
 1404
 1405
 1406
 1407
 1408
 1409
 1410
 1411
 1412
 1413
 1414
 1415
 1416
 1417
 1418
 1419
 1420
 1421
 1422
 1423
 1424
 1425
 1426
- Huang B, Thorne PW, Banzon VF, et al (2017) Extended Reconstructed Sea Surface Temperature, Version 5 (ERSSTv5): Upgrades, Validations, and 1389
 1390
 1391
 1392
 1393
 1394
 1395
 1396
 1397
 1398
 1399
 1400
 1401
 1402
 1403
 1404
 1405
 1406
 1407
 1408
 1409
 1410
 1411
 1412
 1413
 1414
 1415
 1416
 1417
 1418
 1419
 1420
 1421
 1422
 1423
 1424
 1425
 1426

32 *SH zonally asymmetric circulation with cEOF*

- 1427 Intercomparisons. *Journal of Climate* 30(20):8179–8205. <https://doi.org/10.1175/JCLI-D-16-0836.1>
- 1428
- 1429
- 1430 Hufkens K (2020) Ecmwfr: Programmatic interface to the two European
1431 Centre for Medium-Range Weather Forecasts API services
- 1432
- 1433 Irving D, Simmonds I (2015) A Novel Approach to Diagnosing Southern
1434 Hemisphere Planetary Wave Activity and Its Influence on Regional Climate
1435 Variability. *Journal of Climate* 28(23):9041–9057. <https://doi.org/10.1175/JCLI-D-15-0287.1>
- 1436
- 1437 Irving D, Simmonds I (2016) A New Method for Identifying the Pacific–South
1438 American Pattern and Its Influence on Regional Climate Variability. *Journal*
1439 of Climate 29(17):6109–6125. <https://doi.org/10.1175/JCLI-D-15-0843.1>
- 1440
- 1441 Kao HY, Yu JY (2009) Contrasting Eastern-Pacific and Central-Pacific
1442 Types of ENSO. *Journal of Climate* 22(3):615–632. <https://doi.org/10.1175/2008JCLI2309.1>
- 1442
- 1443
- 1444
- 1445 Katz RW, Brown BG (1991) The problem of multiplicity in research on
1446 teleconnections. *International Journal of Climatology* 11(5):505–513. <https://doi.org/10.1002/joc.3370110504>
- 1446
- 1447
- 1448
- 1449 Krokhin VV, Luxemburg WMJ (2007) Temperatures and precipitation totals
1450 over the Russian Far East and Eastern Siberia: Long-term variability and
1451 its links to teleconnection indices. *Hydrology and Earth System Sciences*
1452 11(6):1831–1841. <https://doi.org/10.5194/hess-11-1831-2007>
- 1453
- 1454 L'Heureux ML, Thompson DWJ (2006) Observed Relationships between the
1455 El Niño–Southern Oscillation and the Extratropical Zonal-Mean Circula-
1456 tion. *Journal of Climate* 19(2):276–287. <https://doi.org/10.1175/JCLI3617.1>
- 1456
- 1457
- 1458
- 1459 Lim EP, Hendon HH, Thompson DWJ (2018) Seasonal Evolution of
1460 Stratosphere-Troposphere Coupling in the Southern Hemisphere and Impli-
1461 cations for the Predictability of Surface Climate. *Journal of Geophysical*
1462 *Research: Atmospheres* 123(21):12,002–12,016. <https://doi.org/10.1029/2018JD029321>
- 1463
- 1464 Mo KC (2000) Relationships between Low-Frequency Variability in the
1465 Southern Hemisphere and Sea Surface Temperature Anomalies. *Jour-*
1466 *nal of Climate* 13(20):3599–3610. [https://doi.org/10.1175/1520-0442\(2000\)013<3599:RBLFVI>2.0.CO;2](https://doi.org/10.1175/1520-0442(2000)013<3599:RBLFVI>2.0.CO;2)
- 1467
- 1468
- 1469 Mo KC, Paegle JN (2001) The Pacific–South American modes and their
1470 downstream effects. *International Journal of Climatology* 21(10):1211–1229.
1471 <https://doi.org/10.1002/joc.685>
- 1472

- Nuncio M, Yuan X (2015) The Influence of the Indian Ocean Dipole on Antarctic Sea Ice. *Journal of Climate* 28(7):2682–2690. <https://doi.org/10.1175/JCLI-D-14-00390.1> 1473
 1474
 1475
 1476
 1477
 1478
 1479
 1480
 1481
 1482
 1483
 1484
 1485
 1486
 1487
 1488
 1489
 1490
 1491
 1492
 1493
 1494
 1495
 1496
 1497
 1498
 1499
 1500
 1501
 1502
 1503
 1504
 1505
 1506
 1507
 1508
 1509
 1510
 1511
 1512
 1513
 1514
 1515
 1516
 1517
 1518
- Pezza AB, Rashid HA, Simmonds I (2012) Climate links and recent extremes in antarctic sea ice, high-latitude cyclones, Southern Annular Mode and ENSO. *Climate Dynamics* 38(1):57–73. <https://doi.org/10.1007/s00382-011-1044-y>
- Plumb RA (1985) On the Three-Dimensional Propagation of Stationary Waves. *Journal of the Atmospheric Sciences* 42(3):217–229. [https://doi.org/10.1175/1520-0469\(1985\)042<0217:OTTDPO>2.0.CO;2](https://doi.org/10.1175/1520-0469(1985)042<0217:OTTDPO>2.0.CO;2)
- R Core Team (2020) R: A Language and Environment for Statistical Computing. R Foundation for Statistical Computing, Vienna, Austria
- Raphael M (2003) Recent, Large-Scale Changes in the Extratropical Southern Hemisphere Atmospheric Circulation. *Journal of Climate* 16(17):2915–2924. [https://doi.org/10.1175/1520-0442\(2003\)016<2915:RLCITE>2.0.CO;2](https://doi.org/10.1175/1520-0442(2003)016<2915:RLCITE>2.0.CO;2)
- Raphael MN (2004) A zonal wave 3 index for the Southern Hemisphere. *Geophysical Research Letters* 31(23). <https://doi.org/10.1029/2004GL020365>
- Raphael MN (2007) The influence of atmospheric zonal wave three on Antarctic sea ice variability. *Journal of Geophysical Research: Atmospheres* 112(D12). <https://doi.org/10.1029/2006JD007852>
- Saji NH, Yamagata T (2003) Possible impacts of Indian Ocean Dipole mode events on global climate. *Climate Research* 25(2):151–169. <https://doi.org/10.3354/cr025151>
- Saji NH, Goswami BN, Vinayachandran PN, et al (1999) A dipole mode in the tropical Indian Ocean. *Nature* 401(6751):360–363. <https://doi.org/10.1038/43854>
- Smith AK (1995) Numerical simulation of global variations of temperature, ozone, and trace species in the stratosphere. *Journal of Geophysical Research: Atmospheres* 100(D1):1253–1269. <https://doi.org/10.1029/94JD02395>
- Trenberth KE (1980) Planetary Waves at 500 mb in the Southern Hemisphere. *Monthly Weather Review* 108(9):1378–1389. [https://doi.org/10.1175/1520-0493\(1980\)108<1378:PWAMIT>2.0.CO;2](https://doi.org/10.1175/1520-0493(1980)108<1378:PWAMIT>2.0.CO;2)
- Trenberth KF, Mo KC (1985) Blocking in the Southern Hemisphere. *Monthly Weather Review* 113(1):3–21. [https://doi.org/10.1175/1520-0493\(1985\)113<0003:BITSH>2.0.CO;2](https://doi.org/10.1175/1520-0493(1985)113<0003:BITSH>2.0.CO;2)

34 *SH zonally asymmetric circulation with cEOF*

- 1519 Turner J, Hosking JS, Bracegirdle TJ, et al (2017) Variability and trends in
1520 the Southern Hemisphere high latitude, quasi-stationary planetary waves.
1521 International Journal of Climatology 37(5):2325–2336. <https://doi.org/10.1002/joc.4848>
- 1523
- 1524 van Loon H, Jenne RL (1972) The zonal harmonic standing waves in the south-
1525 ern hemisphere. Journal of Geophysical Research 77(6):992–1003. <https://doi.org/10.1029/JC077i006p00992>
- 1527
- 1528 Walker SGT (1914) Correlation in Seasonal Variations of Weather, III: On the
1529 Criterion for the Reality of Relationships Or Periodicities. Meteorological
1530 Office
- 1531
- 1532 Wickham H (2009) Ggplot2: Elegant Graphics for Data Analysis. Use R!,
1533 Springer-Verlag, New York, <https://doi.org/10.1007/978-0-387-98141-3>
- 1534
- 1535 Wilks D (2011) Statistical Methods in the Atmospheric Sciences, vol 100.
1536 Elsevier, <https://doi.org/10.1016/B978-0-12-385022-5.00022-1>
- 1537
- 1538 Wilks DS (2016) “The Stippling Shows Statistically Significant Grid Points”:
1539 How Research Results are Routinely Overstated and Overinterpreted, and
1540 What to Do about It. Bulletin of the American Meteorological Society
1541 97(12):2263–2273. <https://doi.org/10.1175/BAMS-D-15-00267.1>
- 1542
- 1543 Wirth V (1993) Quasi-stationary planetary waves in total ozone and their
1544 correlation with lower stratospheric temperature. Journal of Geophys-
1545 ical Research: Atmospheres 98(D5):8873–8882. <https://doi.org/10.1029/92JD02820>
- 1546
- 1547 Xie P, Arkin PA (1997) Global Precipitation: A 17-Year Monthly Analysis
1548 Based on Gauge Observations, Satellite Estimates, and Numerical Model
1549 Outputs. Bull Amer Meteor Soc 78 (Accessed on <26-08-2021>)(11):2539–
1550 2558. [https://doi.org/10.1175/1520-0477\(1997\)078<2539:GPAYMA>2.0.CO;2](https://doi.org/10.1175/1520-0477(1997)078<2539:GPAYMA>2.0.CO;2)
- 1552
- 1553 Xie Y (2015) Dynamic Documents with R and Knitr, 2nd edn. Chapman and
1554 Hall/CRC, Boca Raton, Florida
- 1555
- 1556
- 1557
- 1558
- 1559
- 1560
- 1561
- 1562
- 1563
- 1564